TURBOMACHINERY & PUMP SYMPOSIA | VIRTUAL
DECEMBER 8-10, 2020
SHORT COURSES: DECEMBER 7, 2020

ROTORDYNAMIC PERFORMANCE OF A FULLY-PARTITIONED DAMPER SEAL: EXPERIMENTAL AND NUMERICAL RESULTS

Adolfo Delgado
Associate Professor
Texas A&M University
College Station, Texas, USA

Luis San Andrés
Mast-Childs Chair Professor
Texas A&M University
College Station, Texas, USA

Jonathan Thiele
Machinery Design Engineer
Rotoflow an Air Products company
Allentown, PA, USA

Jing Yang
Assistant Research Engineer
Texas A&M University
College Station, Texas, USA

Filippo Cangioli
Senior Applications Engineer
Waukesha Bearings
Rickmansworth, Hertfordshire, UK

Adolfo Delgado is an Associate Professor of Mechanical Engineering at Texas A&M University. His research focuses on rotordynamics, structural vibration, energy dissipation mechanisms, thin film lubrication and fluid structure interaction applied to the design, modeling and improvement of rotating machinery systems and components. Prior to joining Texas A&M, Adolfo was a Research Engineer at the General Electric Global Research Center where he led and worked on multiple initiatives involving improvement of existing rotating equipment and development of new rotor-bearing system architectures and turbomachinery components, such as variable geometry bearings, annular seals, dampers and oil-free bearings. Dr. Delgado received his B.S. in mechanical engineering from Simón Bolívar University, and his M.S. and Ph.D. in mechanical engineering from Texas A&M University.

Luis San Andrés performs research in lubrication and rotordynamics, having produced advanced technologies of hydrostatic bearings for primary power cryogenic turbo pumps, squeeze film dampers for aircraft jet engines, and gas foil bearings for oil-free micro turbomachinery. Luis is a Fellow of ASME and STLE, and a member of the Industrial Advisory Committees for the Texas A&M Turbomachinery Symposia. Dr. San Andrés has educated dozens of graduate students serving the profession with distinction. Dr. San Andrés earned a M.S. in ME from the University of Pittsburgh and a Ph.D. in ME from Texas A&M University. Luis has published over 185 peer reviewed papers in various professional journals and with several papers recognized as best in various international conferences.

Jonathan Thiele received his master of science in mechanical engineering from Texas A&M University in August of 2019. His research at the Turbomachinery Laboratory focused on experimentally evaluating the rotordynamic performance of annular gas seals. He is working for Air Products as a machinery design engineer for the Rotoflow department designing cryogenic rotating equipment. Jonathan's past experience includes manufacture engineering for M7 Aerospace and development of risk based reliability program as an Asset Integrity Analyst for Pinnacle ART.

Jing Yang received her B.S. in Thermal and Power Engineering from Huazhong University of Science and Technology, China in 2010 and Ph.D. degree in Fluid Mechanics from Peking University, China in 2016. After graduation, she worked for three years as a post-doctoral Research Associate at the TEES Turbomachinery Laboratory. Since October 2019 Jing continues at the Turbo Lab as an Assistant Research Engineer. Jing Yang's research mainly focuses on the numerical prediction (computational fluid dynamics and bulk flow model) and experimental verification of the dynamic forced performance of annular pressure seals and fluid film bearings.

Filippo Cangioli is Senior Application Engineer for Waukesha Bearings, Rickmansworth, UK. His current duties focus on the design of fluid-film bearings and seals, rotordynamic analysis and development of analytical models. Dr. Cangioli holds a MSc degree in Mechanical Engineering from University of Florence (Italy) and a PhD in Mechanical Engineering from Politecnico di Milano. His research activities focus on the dynamic characterization of labyrinth and brush seals. Filippo has authored more than 30 scientific papers in journals and conference proceedings.

ABSTRACT

Balance piston seals restrict leakage at the discharge side of single shaft centrifugal compressors. There are multiple types of annular seals including labyrinth seals, textured surface seals such as honeycomb seals and hole-pattern seals, conventional pocket damper seals (PDS), and fully-partitioned damper seals (FPDS). These seals face high pressure differentials with large changes in gas density to develop large radial forces impacting the compressor rotordynamic performance. There is an extensive experimental database available quantifying the dynamic forced performance of labyrinth seals and textured surface seals. On the other hand, an experimental database for PDS and FPDS is limited and prevents a fair and direct comparison of their dynamic force performance against textured surface seals. This lecture presents experimentally derived rotordynamic force coefficients for a FPDS obtained at relevant operating conditions in shaft speed and pressure ratio (exit/inlet) along with a direct comparison to published test data available for a honeycomb seal, similar in size and in operating conditions. The dynamic load tests with the FPDS, 4.5 inch in diameter × 3.37 inch in length, include operation at three shaft speeds (10, 15 and 20 krpm: max surface speed of 120 m/s), a supply pressure of 70 bar(a), three exit/inlet pressure ratios (25%, 50%, 65%), and with circumferential inlet flow pre-swirl conditions ranging from 10% to 160% of shaft surface speed.

Of interest to a damper seal performance is the cross-over frequency, which determines the transition from a negative to a positive effective damping coefficient. The FPDS produces effective damping magnitudes near 10 kN.s/m above the cross-over frequency, which ranges from 28-62Hz and above 70 Hz for the lowest (below 0.1) and highest inlet pre-swirl (above 0.6) conditions, respectively. On the other hand, the FPDS generates small direct stiffness coefficients, varying with frequency though contained within +/- 2 MN/m band. Therefore, the FPDS can significantly improve damping ratio of a compressor rotor-bearing system without shifting the natural frequencies. Comparisons of the force coefficients for the FPDS versus a honeycomb (HC) seal demonstrate that both seals generate comparable effective damping coefficients and similar cross-over frequencies with some differences highlighted in the discussion of the results. As expected from a textured seal, the HC produces much larger direct stiffness coefficients when compared to the FPDS. In terms of leakage performance, the FPDS leaks roughly 20%-25% more than the HC. Experimental results are also compared against predictions obtained from CFD and bulk flow models. The CFD and bulk flow predictions yield a good to moderate correlation to the experimental data depending on the operating conditions of rotor speed and pressure ratio. Both methods represent a viable approach for designing FPDSs and predicting their rotordynamic performance.

INTRODUCTION

Demand for high power density turbomachinery continues to drive the need to accommodate higher pressures and shaft speeds while ensuring a rotor stable operation with acceptable vibration levels. Annular seals play a pivotal role on both the aerodynamic and rotordynamic performance of modern turbomachinery. While the primary role of annular seals is to reduce secondary or parasitic flows, they can generate large radial forces and have a measurable impact on the rotordynamic performance of turbomachinery, particularly in centrifugal compressors. Prior to the infamous Ekofisk instability event [1-3] in 1972, the rotordynamic impact of annular gas seals was largely underestimated. Since this high-profile case study, the role of annular gas seals in compressor rotordynamics received more scrutiny, leading to a significant amount of experimental and analytical work that continues up to the present [4-5].

Labyrinth seals are the most common type of annular gas seal used in turbomachinery. These have been widely implemented as inter-stage and eye-impeller seals. In centrifugal compressors, labyrinth seals were also the primary choice as balance piston seals to face the largest pressure differentials in the machine. Balance piston seals are located at the center of a back-to-back compressor, near the rotor

mid-span, or after the last stage in a straight-through compressor. Because of their location and large pressure differentials, these seals develop the largest destabilizing aerodynamic forces and directly affect the rotordynamic performance of centrifugal compressors. The magnitude of these forces is highly sensitive to the fluid density, pressure difference across the seal, and the inlet circumferential flow velocity or pre-swirl (ratio of incoming tangential flow velocity to rotor surface speed) [6].

In a landmark paper in 1965, Alford [7] explains two of the probable causes for self-excited rotor whirl in aircraft engines. The first one is the non-uniform circumferential static pressure acting on the rotor surface within seal cavities; and the second one is rotor eccentricity causing an unequal circumferential tip blade clearance. The analysis of flow in a labyrinth seal shows that a non-uniform circumferential pressure is responsible for developing tangential destabilizing forces proportional to the radial displacement. Alford concludes that a labyrinth seal having a diverging clearance (tooth clearance increases along the flow direction) is more stable than a converging clearance, and with rotor whirl beginning at a torque level proportional to the rotor bearing system stiffness. Alas, Alford only accounts for axial flow in the analysis, and neglects circumferential flow assuming it had no effect on the pressure distribution within the seal. The assumption proved to be incorrect, as later shown by Benckert and Wachter [8], who demonstrate experimentally that circumferential flow in labyrinth seals directly affects their destabilizing forces. Experiments in [8] consisted of statically offsetting a shaft and measuring the cross-coupled stiffness coefficients for labyrinth seals (see-through and interlocking), labyrinth seals with swirl webs (i.e. swirl brake) at the entrance of the seal to disrupt circumferential flow, labyrinth seals with swirl webs throughout the seal (this can be considered as the first version of a FPDS), and a honeycomb seal. Since their experimental results did not include damping coefficients (i.e. static tests), the authors recommend a labyrinth seals with inlet swirl webs, more so than a labyrinth seal with swirl webs or a honeycomb seal, as the best option to minimize destabilizing forces.

A few years later as part of the engineering work to enable the development of turbopumps for the Space Shuttle Main Engine (SSME), Von Pragenau [9] numerically shows that using a textured (or rough) surface stator in an annular seal results in a lower circumferential flow and axial flow velocities; and consequently, improves the rotordynamic performance and reduces leakage when compared to a seal with smooth surface stator. Although this analysis was completed for incompressible fluid, the improved rotordynamic and leakage performance also applies to compressible fluids as experimentally validated by Childs et al. [10-11]. In addition, textured surface seals can develop large direct stiffness and damping coefficients, i.e., centering and dissipative forces that could stabilize and otherwise unstable machine.

In 1903 Vance and Schultz [12] present the invention of a damper seal calling it the TAMSEAL®. This novel seal, later called pocket damper seal (PDS), provides damping from two distinct features. The first feature is the blade divergent clearance along the length of the seal. The second feature is the buffer walls dividing the circumferential grooves into pockets and thus reducing the circumferential flow. Vance and Li [13] test and present the experimental results for this new damper seal. Shaft speed coast-down tests served to evaluate the seal effectiveness when crossing a critical speed while impact load tests provided data for the estimation of force coefficients. The PDS proves to have significantly more (viscous) damping than a traditional labyrinth seal does.

Figure 1 shows photographs of a labyrinth seal, a honeycomb seal, a hole-pattern seal, and a FPDS. Honeycomb seals have a typical hexagon pattern with thin walls, while hole-pattern seals feature round holes with a certain depth. Similar to labyrinth seals, a PDS features circumferential grooves but also includes circumferential buffer walls running axially, dividing the grooves into multiple pockets. Figure 2 shows a comparison between the conventional PDS and a FPDS. A conventional PDS includes active and inactive segments alternating along the length of the seal. Inactive segments are continuous circumferential grooves similar to those in labyrinth seals (i.e. without buffer walls). The inactive segments in a PDS are plenums maintaining a constant pressure in the cavity during rotor whirl [1, 14]. Active groove segments are segregated with buffer walls. A FPDS includes buffer walls or ribs spanning the entire length of the seal, thus producing only active segments. The PDS may include notches toward the exit blade to enlarge the effective exit clearance, where the FPDS only has a straight through clearance.

The following references focus on the dynamic performance of fully-partitioned pocket damper seals (FPDS) while briefly mentioning work related to textured surface seals. Refs. [4, 6, 15-17] provide a comprehensive review of the performance of textured surface seals.

In 1999, Li et al. [18] create a bulk-flow model (BFM) for a multiple cavity pocket damper seal and uses turbulent flow shear stress parameters based on Moody's pipe friction factors. The authors compare the model to experimental data from Li [19] for a 4-pocket single cavity PDS. Results show the predictions agree with measurements for leakage and direct damping. The model highlights the influence of rotor speed and pressure drop in the seal dynamic force performance. Experimental results also show the PDS has a large damping when compared to that in a similar size labyrinth seal. Li et al. [20] also test a straight-through honeycomb seal and a pocket damper seal, both with a length to diameter ratio (*L/D*) of 0.54, installed with a flexible rotor. The authors test the seals, oriented in a back-to-back configuration, with different shaft eccentricities at a maximum supply pressure of 500 psi and with inlet flow pre-swirl magnitudes ranging from null to 50% of shaft surface speed. The authors only report measurements of direct force coefficients and produce effective stiffness and damping coefficients. The experimental results show that both seals produce a high effective damping, where the honeycomb seal has positive stiffness whereas the PDS has a negative stiffness. The experimental results show the effective damping decreases with shaft (static) eccentricity for both seals.

In 2003, Sprowl [21] reports the experimental results for two seals, a honeycomb seal (HC) and a labyrinth seal, both operating under three pressure ratios, *PR*= 0.15, 0.35 and 0.50, three rotor speeds (10, 15, 20 krpm), and three inlet pre-swirl conditions at 0%, 30% and 60 % of shaft speed. The test rig in Ref. [21] is also used in the current endeavor and described in a later section. The test results show

that the inlet pre-swirl does not affect the seals' effective stiffness, but does evidently affect the effective damping coefficients. Importantly enough, the HC effective direct stiffness drops 68% when the cavities fill in with debris and transits into the performance of a (nearly) smooth surface seal. The effective damping also drops by ~ 25% to 35 %, hence raising the cross-over frequency, which is the whirl frequency where the effective damping changes from a negative to a positive magnitude. The lower the cross-over frequency, the more damping the seal provides, and hence it promotes rotor-bearing system stability.

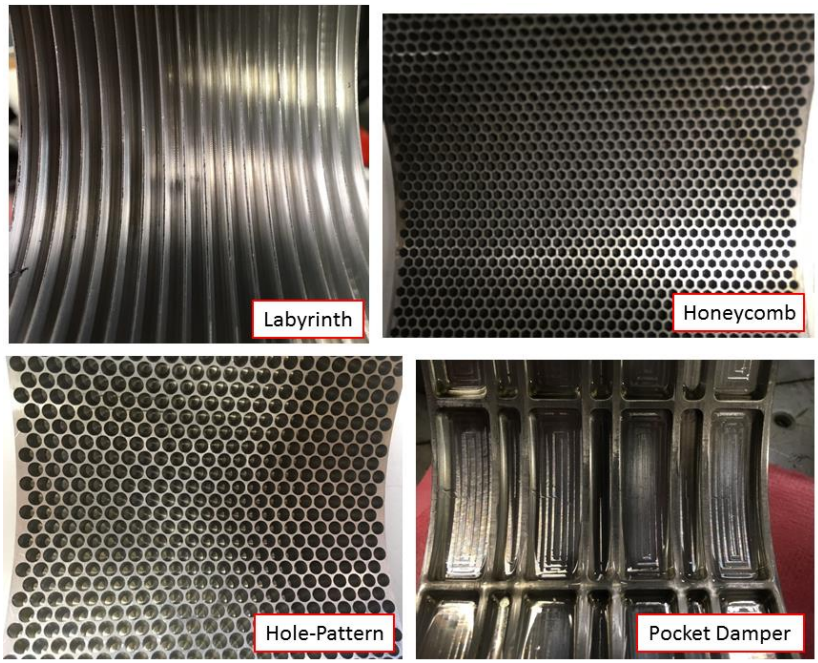

Figure 1 Close-up photographs of a labyrinth seal, a honeycomb seal, a hole-pattern seal, and fully-partitioned pocket damper seal.

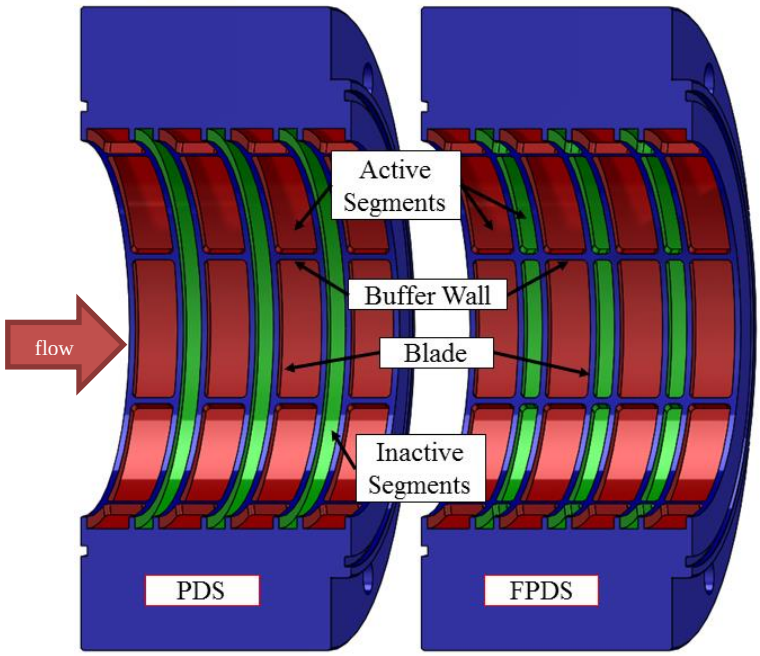

Figure 2 Cut-view of two seals illustrating the differences between a standard PDS and FPDS.

Ertas [22] and Ertas et al. [23] measure the stiffness and damping coefficients of two PDSs, one eight-bladed and the other twelve-bladed. The authors test the seals with a supply pressure up to 70 bar, rotor speeds up to 20 krpm, and excitation frequencies from 20 to 300 Hz. The eight-bladed seal experiences the highest negative magnitude direct stiffness coefficient and a largely positive direct damping coefficient. Both seals produce positive direct damping and same sign cross-coupling stiffness. Results show a conventional PDS, one with active and inactive cavities and a diverging clearance (flow direction) generates a largely negative direct stiffness

coefficient, and whose magnitude reduces with increasing excitation frequency. The same seal but with a straight through clearance also produces a negative direct stiffness at lower whirl frequencies, but transitions into a positive direct stiffness at high frequencies. The change in blades' clearance (exit to inlet) controls the phase and magnitude of the dynamic pressure in the seal cavities, thus affecting the generation of the force coefficients.

Brown and Childs [24] test a hole-pattern seal installed with a negative inlet pre-swirl ring. The seal dimensions are similar to those of the seal investigated by Childs and Wade [25]. The tests are conducted with a 70 inlet bar pressure, shaft speed up to 20 krpm, and pressure ratios from 0.5 to 0.7. Direct force coefficients are not affected by either changing the pressure ratio, or the shaft speed, or the inlet pre-swirl condition. Changing the pressure ratio shows no influence on the seal effective damping coefficient. Cross-coupled force coefficients increase in magnitude with rotor speed and decrease with an increase of a negative inlet pre-swirl. A change in the inlet flow pre-swirl shows little influence on the direct damping coefficients for operation at the highest shaft speed of 20 krpm and under a 50% pressure ratio. The results provide evidence that a negative inlet pre-swirl, i.e., against shaft rotation, helps to stabilize a rotor as determined by increases in the peak effective damping along with a lower cross-over frequency.

Ertas et al. [14] tests labyrinth, honeycomb, and FPDS seals comparing their rotordynamic force coefficients. The authors test all seals with a low pressure ratio and in choked conditions, with a supply pressure of 6.9 bar discharging to atmosphere. All seals experience negative effective damping at low frequencies and increases in magnitude with pre-swirl. The FPDS results display the lowest cross-over frequency when comparing to other seals. With pre-swirl, the labyrinth seal has negative effective damping up to 100 Hz excitation frequency. When comparing both the honeycomb seal and FPDS to the labyrinth seal, the cross-over frequency is greatly reduced, for both of the seals, to 40-60 Hz and the peak effective damping is increased. From the pocket pressure analysis in the FPDS, the pre-swirl demonstrates to be the dominant factor affecting seal stability. With pre-swirl, the effect in destabilizing forces is larger toward upstream than downstream of the seal.

Predictive analyses on the force performance of PDS use two major approaches; the bulk flow model (BFM) [18] and computational fluid dynamics (CFD) model. To date, the BFM albeit simpler and faster, is known to produce inaccurate force coefficients for FPDS; hence, the current trend is to rely on more advanced though complex computational physics models, i.e., CFD. In 2012, Li et al. [26] numerically calculate the leakage and rotordynamic coefficients for an eight-bladed, eight-pocket PDS against the test data in Ref. [23], employing a multi-frequency whirl orbit method and a commercial Reynolds-averaged Navier-Stokes solver. The CFD model predicts the dynamic performance of the PDS operating with supply pressure = 69 bar and pressure ratio (= exit pressure/inlet pressure) PR = 0.52, 0.33, and 0.12, and a rotor speed of 10.2 krpm (surface speed = 61 m/s). For PR = 0.52, the magnitude of the CFD predicted direct stiffness is ~ 2 MN/m greater than the test data for whirl frequencies between 25 Hz to 275 Hz, and the predicted direct damping coefficient agrees with the test data; thus demonstrating the coming of age of CFD to accurately model the forced performance of textured seals.

In 2014, Vannini et al. [27] build a test rig to investigate a labyrinth and pocket damper seals response over negative pre-swirl, differences between single and multi-frequency excitation, and the difference between centered and offset seals. They find that negative pre-swirl shows a stabilizing effect in the seals. Results show testing with a multi frequency excitation proves to have a similar effect to single frequency excitation. Having the seal with a static offset, within 10% of seal clearance, shows negligible effect on the dynamic performance when comparing to a centered seal. The pocket damper seal displays a higher effective stiffness and damping coefficients when compared to the labyrinth seal.

Li et al. [28] in 2015 conduct CFD analyses to quantify the effects of PR, rotor speed, and inlet circumferential flow pre-swirl on the leakage and dynamic force coefficients for the test FPDS in Ref. [14]. The flow in the FPDS is choked for operation with a supply pressure = 6.9 bar and exit pressure = 1 bar. Whereas an increase in the seal inlet pressure produces a large increase of the seal direct stiffness and damping coefficients, changes in exit pressure have a minor influence on the seal dynamic forced performance. As the rotor speed increases, both direct stiffness and damping coefficients grow slightly. Lastly, an increase in the seal inlet circumferential velocity enlarges the seal cross-coupled stiffness, hence reducing the seal effective damping coefficient.

Vannini et al. [29] present in 2015 a case study with experimental measurements and theoretical results from a single stage compressor for a wet-gas compression application. Wet-gas refers to the presence of liquid within a mostly air volume. The labyrinth seal predictions results agreed with the experimental sub-synchronous vibration experienced in the compressor in field operation. CFD contour plots were created, showing swirl is significant in the labyrinth seals. Inserting a fully-partitioned pocket damper seal into the CFD model theoretically reduces swirl, but in effect causes a higher leakage than the labyrinth seal. Their choice in reducing the vibration was decided a higher priority than leakage.

Cangioli et al. [30] (2020) develop a two-control-volume BFM that considers both the circumferential and recirculating flows within a pocket. The authors employ the test rig in Ref. [27] to measure the dynamic force coefficients of an eight-rib FPDS, operating with supply pressure = 67 bar and discharge pressure = 50 bar, and at rotor speed = 10 krpm (surface speed 115 m/s). The test seal inlet pre-swirl ratio is ~ ± 1. The BFM predicted direct stiffness coefficient and direct damping coefficient is ~ 45% and ~ 15% larger (at maximum) respectively than the test results for the two pre-swirl ratios. The BFM in [30] is considered the best to date.

There is an extensive experimental database available for labyrinth seals and textured surface seals (honeycomb and hole-pattern) [4]. However, there is no such database for FPDS to compare against those of the textured seals. This work aims to provide an experimental data set to enable a direct comparison of the dynamic performance of a FPDS versus that of a honeycomb seal, and evaluates the accuracy

of existing models (bulk flow and CFD) to predict FPDS force coefficients. The experimental results were obtained with a conventional FPDS design in a controlled motion test rig [21] described in the next section. This same rig that hosted the textured surface seals [4] is used for comparison.

EXPERIMENTAL SET UP AND PROCEDURE

The test facility

Figure 3 shows a cross-section of the controlled-motion test rig detailing its main components [21]. The test stand was originally designed and built in 1992 to perform dynamic force testing on hydrostatic bearings [26], and later used to test both liquid seals and gas seals. The rig consists of a long solid steel rotor, 114.3 mm (4.5") in diameter (*D*), supported on silicon oil-lubricated hydrostatic bearings. Lateral pedestals host the hydrostatic bearing housings and include instrumentation to measure the lubricant supply pressure delivered by a feed pump and the temperature of the bearings. A variable frequency drive motor drives the rotor through a 1:7 speed increaser and a disk-pack flexible coupling. The support pedestals are 15" (380 mm) apart to host a flexibly-mounted stator assembly in between.

Figure 4 shows a recent photograph of the rig and a close-up view of the test section. Structural beam elements surrounding the entire test section support a pair of electrohydraulic shakers, horizontal (steel cables) and vertical stiffeners (coil springs). The stiffeners prevent static instabilities as annular seals can develop negative direct stiffnesses and/or cross-coupled damping coefficients that can yield an effective *centering* stiffness that is negative. The two shakers, positioned 45º from the vertical (90º apart), excite the stator assembly at prescribed amplitudes and frequencies. A set of three pitch stabilizers (turn-buckles) connect each side of the stator to the bearing pedestals providing lateral compliance and the means to center and align the stator respect to the rotor.

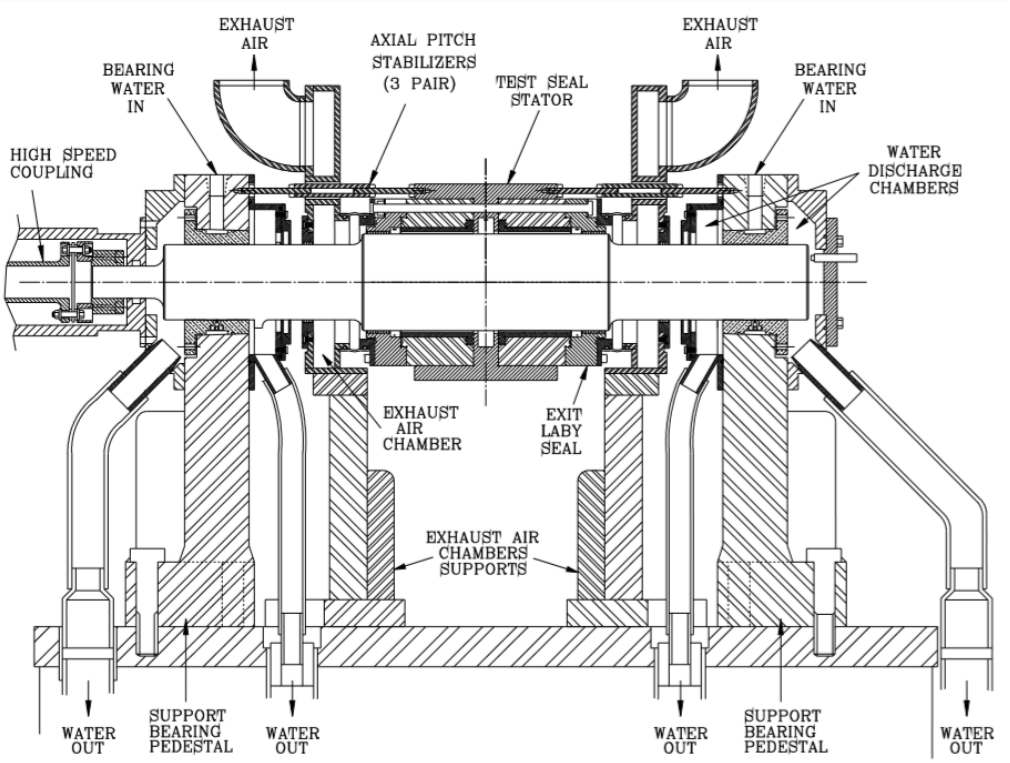

Figure 3 Cross-section of test rig stand depicting main components [21].

Figure 5 depicts a three dimensional (3D) partial cut view of the stator assembly including the instrumentation and main components. The stator houses a pair of test seals in a back-to-back configuration with high pressure air supplied at its center so as to balance any axial thrust. Pressure transducers measure the supply pressure at the stator inlet and the seal exit plane. A pitot tube located at the seal inlet provides static and total pressure measurements to estimate the inlet circumferential flow velocity. Figure 5 also shows detailed views and design parameters of the three pre-swirl rings used to vary the circumferential flow velocity at the inlet of the seals. The "low" pre-swirl ring injects the flow radially at the seal inlet plane, whereas the "mid" and "high" pre-swirl rings inject the flow at an angle in the direction of rotation. Two nine teeth labyrinth seals (.178mm/0.007" radial clearance, 28.5 mm/1.125" in length) with inlet swirl brakes seal the stator ends and allow for pressurization of the test seals' discharge cavity. This feature allows adjusting the pressure ratio across the seal for a given supply pressure. Accelerometers, located orthogonally to each other, measure the acceleration of the stator assembly. Four Eddy-current sensors or proximity probes, also orthogonal to the accelerometers, measure the position of the stator in reference to the rotor shaft. Temperature probes are located at the inlet, seals' outlets, and in the piping system.

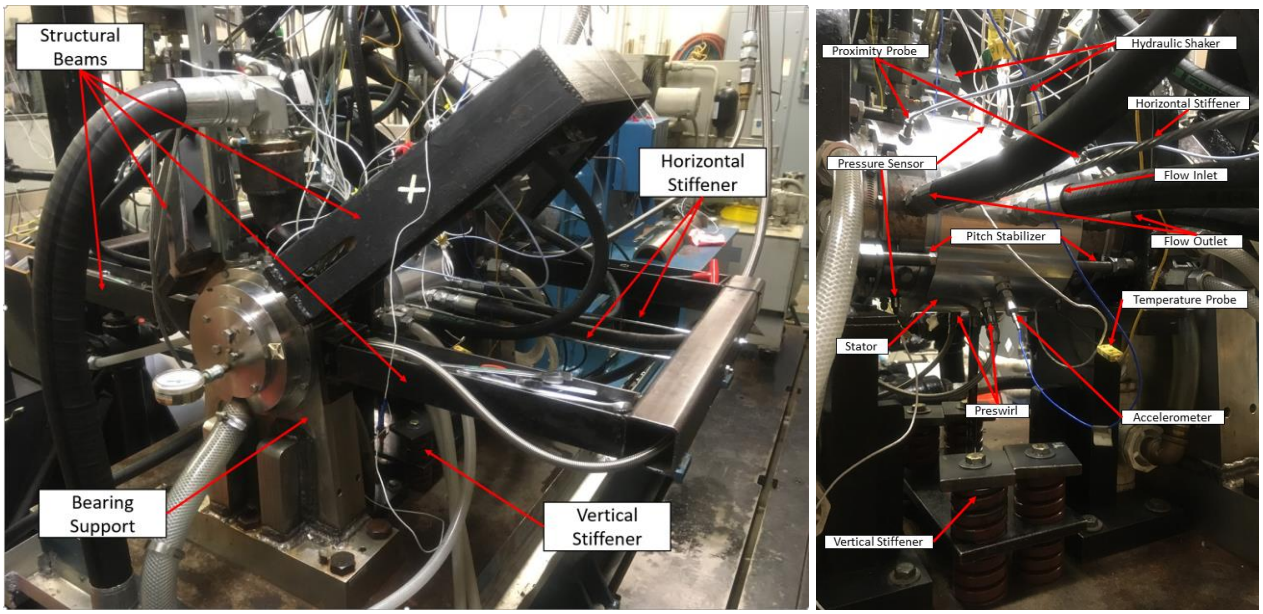

Figure 4 Close-up of the test section depicting stator assembly components.

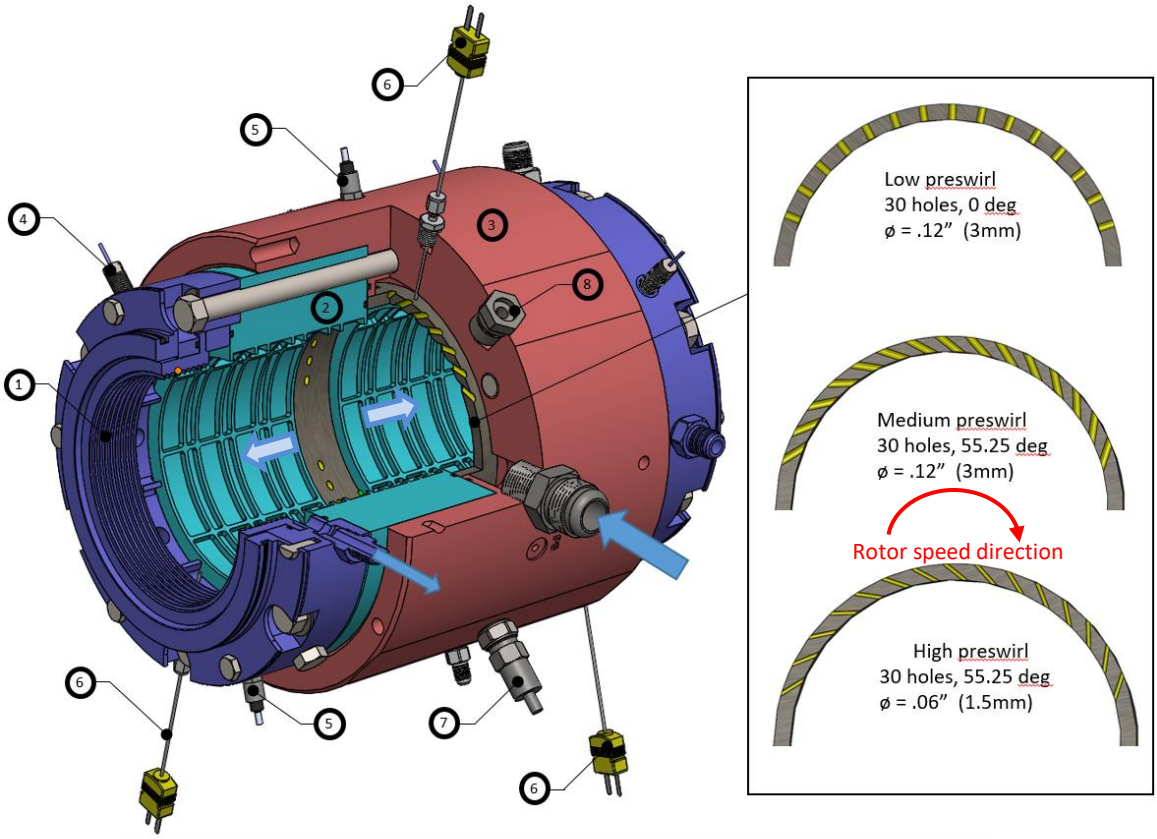

1. End laby seal (with swirl breaks)	2. Test seal	3. Seal housing
4. Proximity probe	5. Static pressure sensors	6. Temperature probes
7. Accelerometers	8. Shaker attachment interface	

Figure 5 Partial cut view of the stator assembly housing two identical test seals, instrumentation and main components including the three inlet pre-swirl rings used to vary inlet circumferential flow.

The test seal

Figure 6 depicts a cut-view of the test seal, a FPDS with all segments active, made of high-strength aluminum (7071-T6) and with a radial clearance of 203 μm [0.008"]. The seal features seven rows with eight (43º) cavities each. Recall the test rotor is 115 mm (4.5 inch) in diameter D and the seal has an overall length L = 85.7 mm (3.37 inch). The test seal design geometric parameters are similar to those of other seals previously machined and tested by Ertas et al. [14] and Vaninni et al. [29] for use in actual compressor applications.

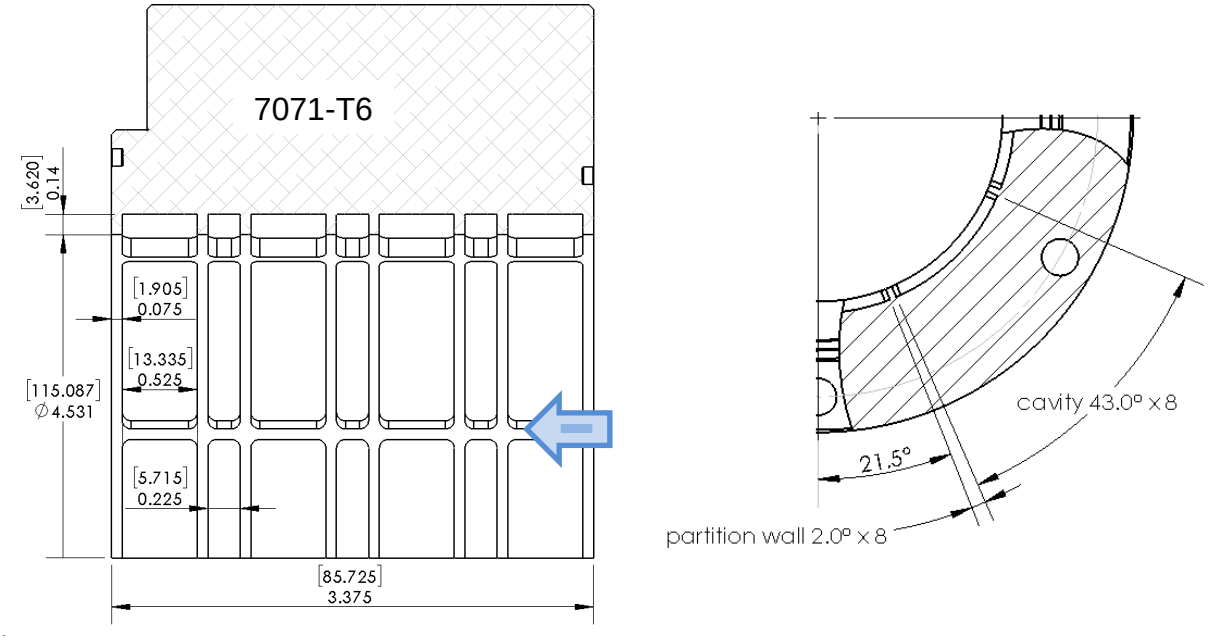

Figure 6 Cut-view of test FPDS depicting seal dimensions in [inch] mm.

Experimental procedure

Table 1 shows the test matrix including three rotor speeds (max. 20 krpm or 120 m/s shaft surface speed), a gas (air) inlet pressure (P_{in}) at 70 bar(a), three exit/inlet pressure ratios, and installations with the three distinct pre-swirl rings. The inlet pressure (P_{in}) and discharge pressure (P_{out}) at the seal exit plane are first adjusted before bringing the rotor to a desired speed. Note that the pressure ratio PR = (P_{out}/P_{in}). The first test condition, for any pre-swirl flow condition, is PR = 25% with the rotor operating at 10 krpm (surface speed of 60 m/s). This specific test condition (PR = 0.25), having P_{in} = 70 bar and P_{out} = 17.5 bar, likely produces a choked flow.

Following the experimental and identification procedure described in Ref. [31] and once the test system reaches a steady state condition, the electro-hydraulic shakers produce a pseudorandom frequency excitation sequentially along each axis, X and Y. The external force excitation lasts ~30 s to produce 10 x 3 s averages, and it is repeated three times for forced excitations along each axis. The procedure continues for operation with the rotor turning at 15 krpm and 20 krpm (surface speed of 120 m/s), before adjusting the discharge pressure (P_{out}) to achieve the next pressure ration (PR).

Assuming small amplitude motions and a centered operation, the seal reaction forces (F_x, F_y) equal

$$-\begin{bmatrix} F_X \\ F_Y \end{bmatrix} = \begin{bmatrix} K & k \\ -k & K \end{bmatrix} \begin{bmatrix} X \\ Y \end{bmatrix} + \begin{bmatrix} C & c \\ -c & C \end{bmatrix} \begin{bmatrix} \dot{X} \\ \dot{Y} \end{bmatrix} \tag{1}$$

Above $X_{(t)}$ and $Y_{(t)}$ are the measured displacements of the stator housing relative to the spinning rotor and its time derivatives. Eq. (1) characterizes the seal forced response with frequency dependent stiffness (K, k) and damping (C, c) force coefficients. The experimental parameters follow from the test system complex dynamic stiffness functions after subtracting the test rig structural stiffness, residual damping and stator mass [31].

Table 1. Test Matrix with fully partitioned pocket damper seal.

Inlet pressure	Inlet Temperature	Exit pressure	Exit/Inlet Pressure ratio [-]	Rotor speed	Rotor surface speed	Pre-swirl ring
70 bar-a (1015 psia)	8-14 ºC (46-67 ºF)	17.5 bar-a (254 psia)	0.25	10 krpm	60 m/s	**Low, medium and high**
		35 bar (508 psia)	0.50	15 krpm	90 m/s	
		45.5 bar (660 psia)	0.65	20 krpm	120 m/s	

NUMERICAL METHODS FOR PREDICTION OF SEAL FORCED RESPONSE

Computational Fluid Dynamics method

A commercial computational fluid dynamics (CFD) software [32] solves the Reynolds-Averaged Navier-Stokes equations (RANS). The turbulence flow model is a standard k-ε model with a scalable wall function. The circumferential speed of the fluid is set as zero at the inlet of the upstream section, except at the bottom wall that represents the spinning rotor with surface speed (ΩR). The inlet pressure (P_{in}) and exit pressure (P_{out}) are specified at the seal inlet and outlet planes respectively. A non-slip flow condition applies to both the shaft and stator surfaces. Based on the measured temperature in tests, the supply temperature is set at ~ 10°C (283 K).

Figure 7 displays the three-dimensional mesh constructed with additional upstream and downstream sections to the FPDS. The mesh node count is about 6.2×10^6. A grid independence analysis employs a finer mesh with node count ~ 8.1×10^6 and proves the medium mesh (node amount ~ 6.2×10^6) is good enough to produce accurate leakage and dynamic force coefficients. Details on the grid independence analysis are not shown here for brevity. See Ref. [33] for details on the grid independence analysis for a PDS.

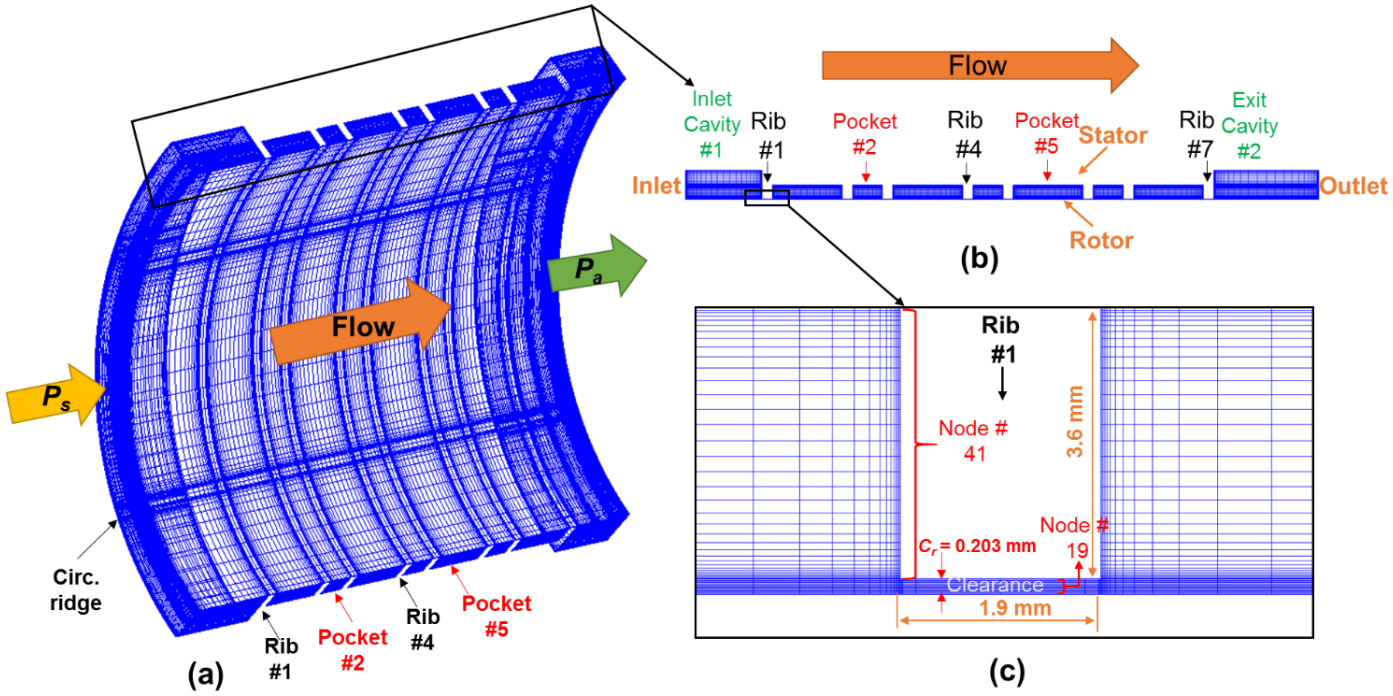

Figure 7 Three-dimensional mesh for an eight-rib fully partitioned damper seal. (a) ¼ cut (90°) of three-dimensional mesh; (b) a cross-section view of the mesh; and (c) mesh details around the first rib (#1) (*L/D* = 0.75, clearance = 0.203 mm).

As to the CFD predictions of dynamic force coefficients for a FPDS, an unsteady state flow model implements a multi-frequency, elliptic orbit method [26] and mesh deformation technique for rotor whirl motion with a known displacement. The coordinates for the rotor elliptic orbit are

$$X_{(t)} = a\sum_{j=1}^{N}\cos(\omega_j t) = a\sum_{j=1}^{N}\mathrm{Re}\left(e^{i\omega_j t}\right);\quad Y_{(t)} = b\sum_{j=1}^{N}\sin(\omega_j t) = -ib\sum_{j=1}^{N}\mathrm{Im}\left(e^{i\omega_j t}\right) \tag{2}$$

where (X, Y) represent rotor center displacements along radial and tangential directions; ω_j stands for a range of excitation frequencies (j = 1, 2, … N); and the amplitudes a = 0.1 C_r/N, b = ½ a. Above i is the imaginary unit. Here, $\{\omega_j\}$ = 2π {25 Hz, 50 Hz… 350 Hz} (N = 14). A Discrete Fourier Transformation turns these displacements and reaction forces into the frequency domain. The relationship equation between the seal reaction force and rotor displacements is

$$-\begin{bmatrix} \bar{F}_x \\ \bar{F}_y \end{bmatrix}_{(\omega_j)} = \begin{bmatrix} H_{(\omega_j)} & h_{(\omega_j)} \\ -h_{(\omega_j)} & H_{(\omega_j)} \end{bmatrix} \begin{bmatrix} \bar{X} \to a \\ \bar{Y} \to -ib \end{bmatrix} \tag{3}$$

where H and h represent the complex direct and quadrature dynamic stiffnesses. The seal dynamic force coefficients are derived at a given frequency as

$$H_{(\omega_j)} = \left(K_{(\omega_j)} + i\,C_{(\omega_j)}\omega_j\right) \leftarrow \frac{\left(a\,F_x - i\,b\,F_y\right)_j}{(a^2 - b^2)}, \quad h_{(\omega_j)} = \left(k_{(\omega_j)} + i\,c_{\omega_j}\right)\omega_j \leftarrow \frac{\left(aF_y + i\,b\,F_x\right)_j}{(a^2 - b^2)}; \; {}_{j=1,\ldots,N} \tag{4}$$

Above (K, k) denote the seal direct and cross-coupled stiffnesses, and (C, c) represent the direct and cross-coupled damping coefficients.

The Bulk-Flow Model

The bulk-flow model (BFM) used for predicting the FPDS static and dynamic forced performance is the one introduced by Cangioli et al. [30]. The model assumptions arise from the flow patterns observed through CFD by Vannini et al. [29]. The pocket separation ribs in the circumferential direction and the teeth or blades along the axial direction generate a flow-path characterized by a jet-flow under the teeth and a recirculating flow within the pockets and in the cavities in between.

Figure 8 illustrates the flow pattern within the FPDS cavities and the control volumes used for modeling the two flow regions. The model relies on boundary layer theory to estimate the recirculating flow area and a friction factor correlation to evaluate the dissipation of the circumferential velocity. The model numerically solves the continuity, circumferential momentum and energy equations using a perturbation method. The dynamic coefficients result from the integration the dynamic pressure and rotor shear stresses along the circumferential direction.

The BFM has been successfully validated in [30]. The results show accurate predictions compared to test data in terms of dynamic force coefficients and leakage flow rate for a seal geometry and operating conditions representative of balance piston seals used in medium-pressure centrifugal compressors.

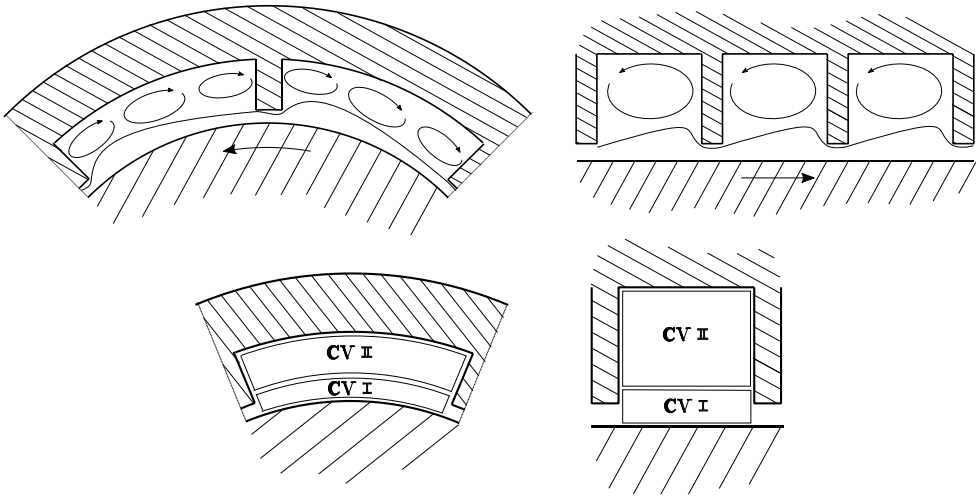

Figure 8. Scheme of the flow patterns and control volumes for BFM analysis of pocket damper seals [30].

EXPERIMENTAL RESULTS AND COMPARISONS TO OTHER TEST DATA

Fully-partitioned damper seal (FPDS)

This section presents the FPDS force coefficients obtained from the multiple test conditions listed in Table 1. Table 2 presents the circumferential inlet pre-swirl ratio (α) obtained with each of the pre-swirl rings and for each of the test conditions. The swirl ratio (α) equals the measured inlet circumferential speed of the gas divided by the rotor surface speed (½ $D\Omega$).

Irrespective of the operating PR, the recorded pre-swirl ratios (α) demonstrate that the rings termed as medium and high pre-swirls produce the same inlet circumferential flow speed. The low-swirl ring ratio is very effective at it gives $\alpha \sim$ 5%-6% of rotor surface

speed. On the other hand, the two other rings, medium and high pre-swirls give α=1.16 → 0.7 and 1.26 → 0.64 as the shaft speed doubles from 10 krpm to 20 krpm.

Table 2. Measured inlet pre-swirl ratio (α) at each test condition.

Inlet pressure [bar]	Exit pressure [bar]	Exit/Inlet Pressure ratio *PR*	Rotor speed [krpm]	Pre-swirl ratio, *a* [-]	Pre-swirl ring [-]
70.6-70.5	19.4-44.7	0.27-0.63	10	0.063	**Low**
70.9-70.4	19.4-46.5	0.28-0.56	15	0.056	
70.7-70.1	18.6-46.4	0.26-0.66	20	0.050	
69.3-70.5	19.2-46.4	0.28-0.66	10	1.16	**Medium**
70.7-71.0	19.0-46.4	0.27-0.65	15	0.74	
70.5-70.3	18.9-46.5	0.27-0.66	20	0.66	
71.0-70.9	18.5-46.5	0.26-0.65	10	1.266	**High**
70.7-70.5	18.4-46.2	0.26-0.65	15	0.843	
70.9-70.6	18.6-46.2	0.26-0.65	20	0.64	

While balance piston seals (any type) are expected to be installed with a swirl brake (or even shunt-injection), the wide range of inlet pre-swirl obtained, α ranging from 5% to 160%, aim at evaluating the sensitivity of the PFDS force coefficients to the magnitude of the inlet circumferential flow speed. The seal performance variation with inlet pre-swirl may drive the selection of the seal type and the design of the swirl mitigation device.

Figures 9 through 12 present the direct stiffness (K), cross-coupled stiffness (k), direct damping coefficient (C), and the effective damping (C_{eff}) and stiffness (K_{eff}) for the FPDS, respectively, versus excitation frequency (ω). Each figure is arranged into a three by three matrix of graphs. Each graph contains test data for three pressure ratios PR= 0.25, 0.50 and 0.65. A dark dashed line represents the rotor speed and separates the results into regions of sub-synchronous whirl and super-synchronous whirl.

In Figures 9-12, each column, from left to right, represents rotor speed increasing: 10 krpm, 15 krpm, and 20 krpm. Each row, from top to bottom, represents the inlet pre-swirl increasing as low, medium, and high pre-swirl rings.

Figure 9 shows the test seal direct stiffness (K) vs. excitation frequency. The left scales present magnitudes in SI units (N/m) while the scales on the right show values in US units (lbf/in). In general, for the three inlet pre-swirl conditions and *PRs*, K increases with frequency, albeit $K < 0$ as $\omega \rightarrow 0$ for the lowest PR=0.25. The largest K magnitude appears for the test condition with the largest rotor speed (20 krpm) and at a synchronous frequency (ω=Ω) and both the low and middle inlet swirl conditions. On the other hand, tests with the high pre-swirl condition produce a direct stiffness K that actually decreases and turns negative at the highest end of the excitation frequencies. Note that rotor speed, 15 krpm and 20 krpm, does not have a large influence on the seal direct stiffness K.

Presently, a $K < 0$ poses no major concern as per affecting (reducing) the natural frequency of an actual rotor-bearing system. Note that the test seal $|K|$ is small enough relative to (say) the direct stiffness of a (mineral oil lubricated) tilting pad bearing.

For the low and middle inlet pre-swirl conditions, Figure 10 shows the cross-coupled stiffness (k) varies little with excitation frequency (ω) or the pressure ratio (PR) and proportionally grows with both shaft speed and inlet pre-swirl. Alas for the high inlet pre-swirl condition, k is a strong function of the PR since as the pressure ratio decreases the cross-stiffness increases. Note that for high frequencies (ω > 200 Hz), k sharply decreases. Please do note the test FPDS produces $k > K$, in particular for operation with the high inlet pre-swirl condition.

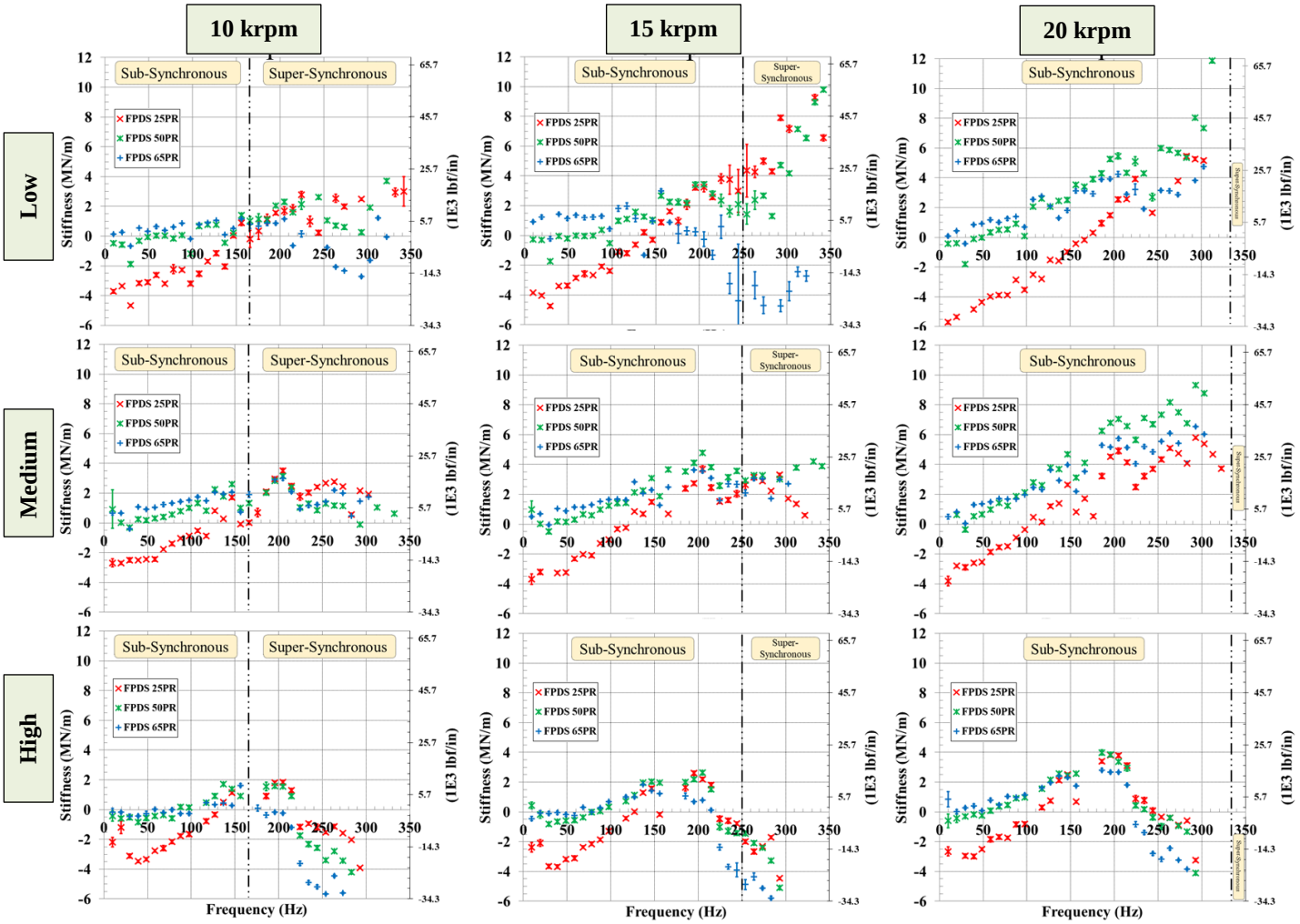

Figure 9 FPDS direct stiffness coefficient (*K*) versus excitation frequency for tests at three pressure ratios (25%, 50%, 65%), three inlet pre-swirls (low, medium, high), and three rotor speeds (10, 15, 20 krpm).

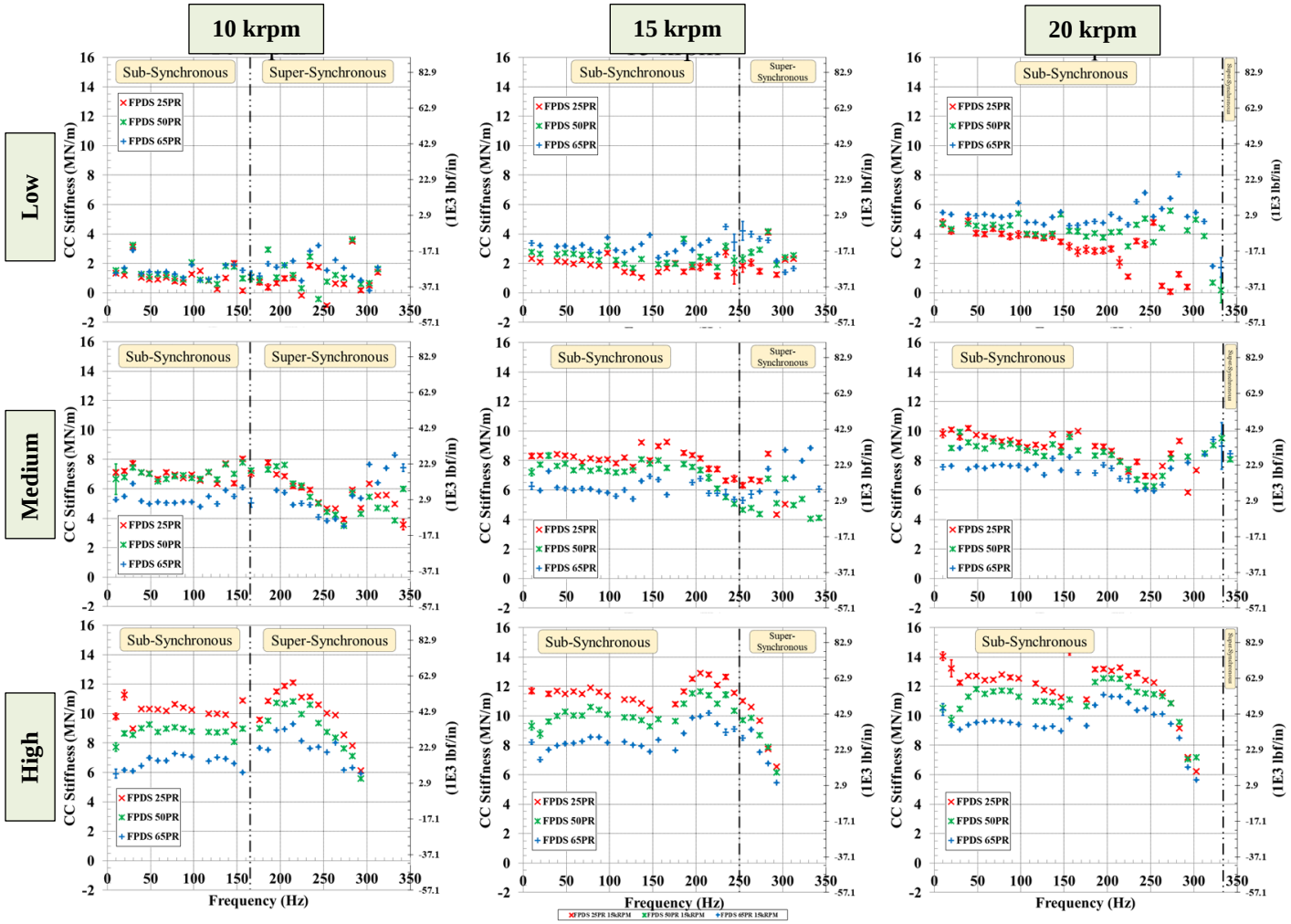

Figure 10 FPDS cross-coupled stiffness coefficient (*k*) versus excitation frequency for tests at three pressure ratios (25%, 50%, 65%), three inlet pre-swirls (low, medium, high), and three rotor speeds (10, 15, 20 krpm).

Figure 11 shows the test seal direct damping coefficient (C) is relatively independent of either rotor speed or excitation frequency or even pressure ratio (PR). However, do note an increase in damping (C) of ~25% at a low excitation frequency for the operating condition with the high inlet pre-swirl, shaft speed equal to 15 krpm and PR=0.25.

The performance of a FPDS is best assessed with the aid of the effective damping (C_{eff}) and stiffness (K_{eff}) coefficients defined as [3]

$$C_{eff} = C - k/\omega, \quad K_{eff} = K + c\,\omega \tag{5}$$

Figure 12 shows the effective damping coefficient versus excitation frequency. C_{eff} combines the stabilizing and destabilizing contributions of the direct damping (C) and cross-coupled stiffness (k), respectively. The results show negative (destabilizing) effective damping coefficients increasing rapidly with excitation frequency. The cross-over frequency (ω_{co}), defining the transition between negative to positive effective damping, increases with increasing rotor speed and inlet pre-swirl. At 20 krpm, the cross-over frequency increases from roughly 60 Hz to 120 Hz, when transitioning from the low to high pre-swirl conditions. For low excitation frequencies, the effective damping magnitudes are negative as is also the case for textured seals. The magnitudes at low frequencies grow with rotor speed and pre-swirl.

Incidentally, irrespective of the operating conditions, the measured cross-coupled damping coefficient (c) are relatively small; hence, $K \approx K_{eff}$. Thus, neither c nor K_{eff} are shown.

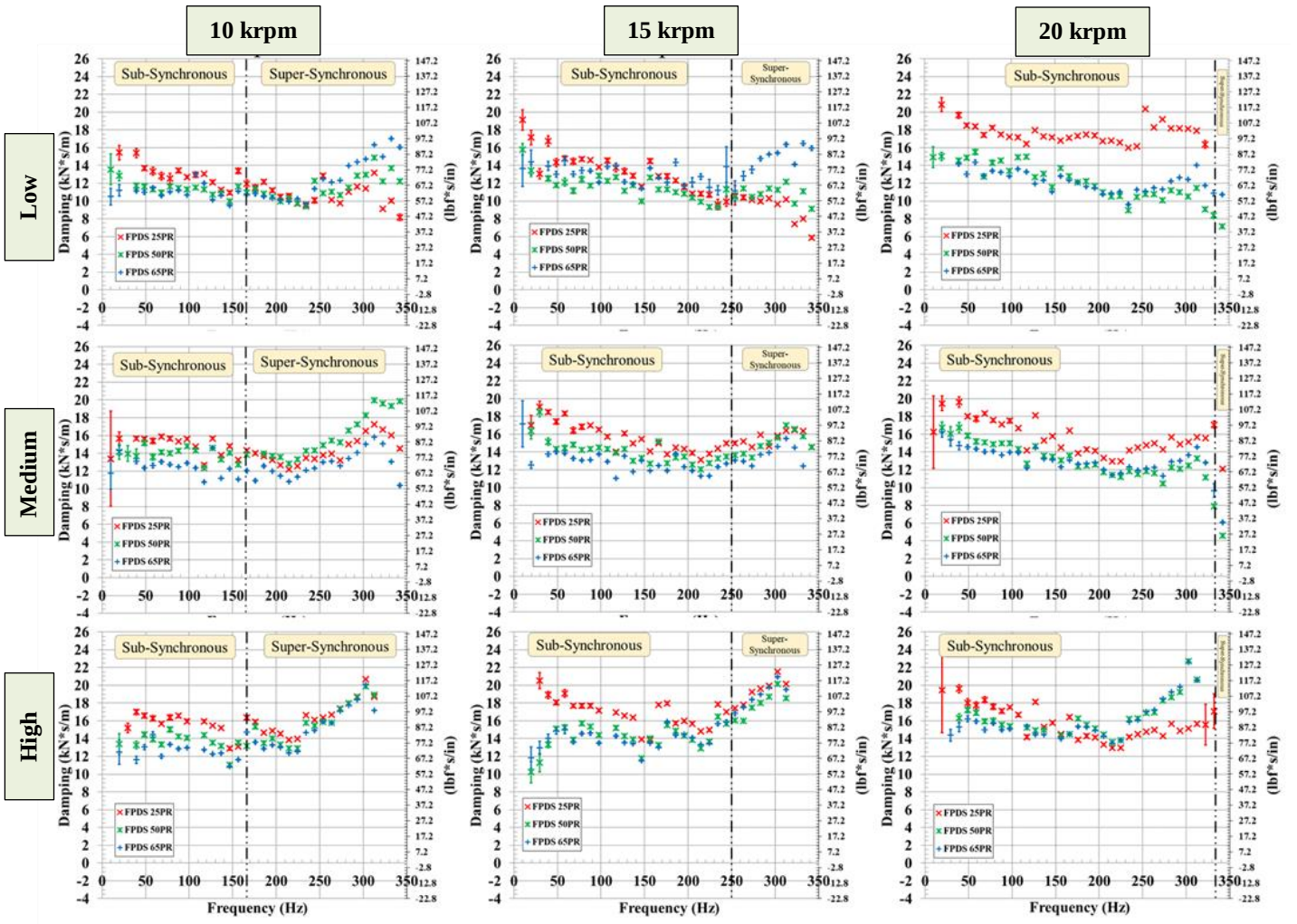

Figure 11 FPDS direct damping coefficient (*C*) versus excitation frequency for tests at three pressure ratios (25%, 50%, 65%), three inlet pre-swirls (low, medium, high), and three rotor speeds (10, 15, 20 krpm).

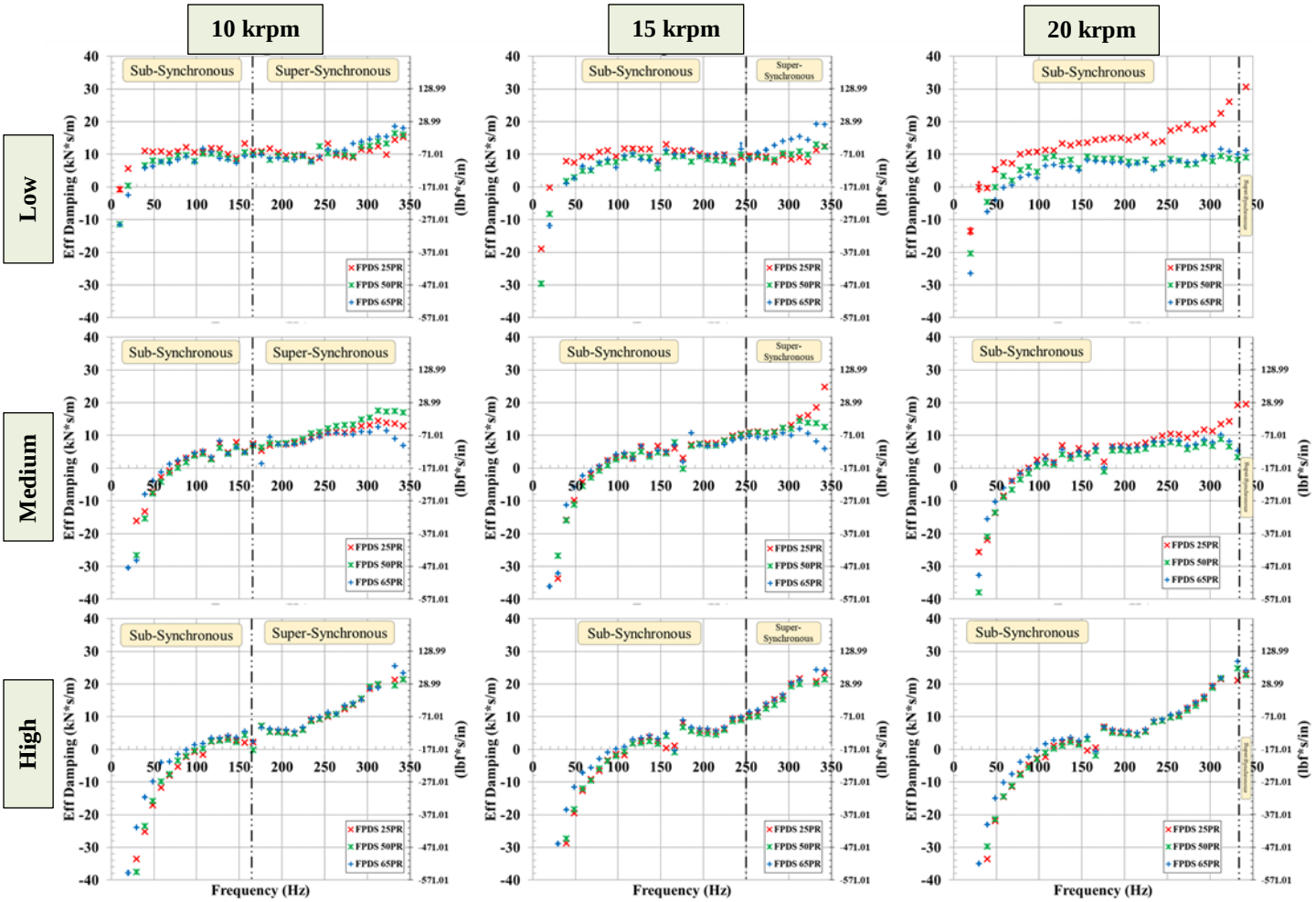

Figure 12 FPDS effective damping coefficient (C_{eff}) versus excitation frequency for tests at three pressure ratios (25%, 50%, 65%), three inlet pre-swirls (low, medium, high), and three rotor speeds (10, 15, 20 krpm).

Figure 13 shows the FPDS leakage versus pressure ratio (*PR*). Each data point represents the mean value from operation at three shaft speeds (10, 15, 20 krpm) for the FPDS installed with the medium and high pre-swirl rings[1]. The small error bars, displaying the standard deviation, show a minute variation in leakage due to changes in surface speed and inlet pre-swirl. As expected, the seal leakage increases with a reduction in *PR* since the pressure drop across the seal increases.

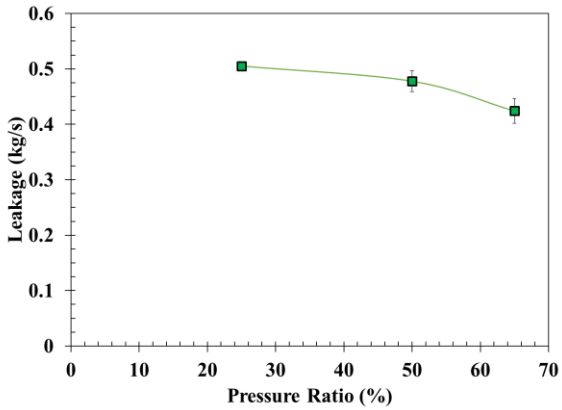

Figure 13 FPDS leakage versus pressure ratio (*PR*). Mean value from tests conducted at three shaft speeds (10, 15, 20 krpm). Seal installed with the medium pre-swirl ring and the high pre-swirl ring.

1 The leakage obtained for the FPDS with the zero pre-swirl ring is significantly larger (30-40%) than the one shown in the Figure. Based on prior experimental evidence and numerical predictions, the mass flow rate measurements with the zero pre-swirl ring are regarded as inaccurate.

Comparison of force coefficients for the fully partitioned pocket damper seal against those of a honeycomb seal and a labyrinth seal

This section presents a comparison of the force coefficients of the current FPDS and compares them against those for a honeycomb seal (HC) [21] and for a labyrinth seal (LS) [34]. Sprowl [21] in 2003 performed measurements in a HC installed in the same experimental facility and identified the seal force coefficients. In the same year, Picardo [34] had obtained force coefficients for the LS. Table 3 lists the geometric dimensions for the three seals and reveals the seals have identical slenderness ratio (L/D) = 0.75 and the same clearance to diameter ratio (C_r/D=0.017).

Table 3. Dimensions for three annular seals: FPDS, a honeycomb seal (HC) and a labyrinth seal (LS).

Parameter	FPDS		HC [21]		LS [34]	
	mm	in	mm	in	mm	in
Seal Diameter, D	115.1	4.53	114.7	4.52	114.7	4.52
Radial clearance, C_r	2.03	0.08	2	0.08	2	0.08
Cavity/Cell width	13.3/5.7	0.52/0.22	0.79	0.03	4.3	0.17
Cavity/Cell depth	3.6	0.14	3.2	0.13	4.3	0.17
Seal L/D	0.75		0.75		0.75	
D/C_r	56.7		57.3		57.3	
Number of blades	8		N/A		20	

For comparison purposes, the stiffness and damping force coefficients are normalized with respect to the pressure drop ($\Delta P=P_{in}-P_{out}$), projected area (L x D), radial clearance (C_r), and shaft rotational speed (Ω) [21]

$$K^* = K\left(\frac{C_r}{\Delta P \cdot D \cdot L}\right),\ C^* = C\left(\frac{C_r * \Omega}{\Delta P \cdot D \cdot L}\right) \tag{6}$$

Figures 13 and 14 depict the normalized force coefficients obtained for three seals: the current FPDS, the HC, and the labyrinth seal (LS). The operating conditions as per supply pressure and shaft speed are identical, whereas the outlet/inlet pressure ratios equal PR = 0.1, 0.3, and 0.5 for the HC, PR = 0.16, 0.3 and 0.52 for the LS, and PR = 0.25, 0.50 and 00.65 for the FPDS. The labyrinth seal (LS) force coefficients are presented for reference only. This seal has coefficients' magnitudes much lower to those for the other two seals, HC and FPDS.

The data shown in the figures below is arranged into a three row by two columns graphs. Each row of graphs shows test data at each rotor speed increasing from 10 krpm (top) to 20 krpm (bottom). The columns represent two coefficients, stiffnesses K and k in Figure 13, and direct damping, C and C_{eff}, in Figure 14.

Figure 14 shows the direct and cross-coupled stiffnesses, K* and k*, versus excitation frequency (ω) for tests obtained with the low pre-swirl ring[2] (pre-swirl ratio $\alpha < 0.1$). In each graph the dash vertical line denotes the rotor angular speed (ω=Ω). The honeycomb seal shows a significant direct stiffness (K*) that hardens with frequency (ω) and increases as the pressure ratio (PR) decreases, PR = 0.50 → 0.15, i.e., as the pressure difference (inlet – exit) increases. On the other had the FPDS shows a minute K*, though positive, whereas the labyrinth seal offers a negligible direct stiffness. Incidentally, only at a high frequency (ω>Ω) and for operation at the top speed of 20 krpm, the FPDS produces a sizable –though still small- centering stiffness K* and not affected by the operating PR.

The three seals (FPDS, HS and LS) produce a cross-coupled stiffness that is a fraction of the corresponding direct stiffness, i.e., $k^* < K^*$. The labyrinth seal has the smallest k* ~0, whereas the cross-coupled stiffness for the HC and FPDS decreases with excitation frequency. The HC shows the largest k* and which appears to increase with shaft speed. For both the HC and the FPDS, an increase in pressure ratio does show a modest increase in k*. Lastly, note the scatter in k* for the FPDS for ω > 200 Hz and shaft speed = 15 krpm (250 Hz) and 20 krpm. At these conditions the FPDS produces a cross-stiffness larger than that for the HC. The magnitude of k* increases as PR rises.

[2] A one-to-one comparison of the force coefficients is not shown for tests conducted with the medium and high preswirl rings. While the preswirl rings are the same for all the seals, the actual swirl ratio is a function of the seal leakage, which affects the pressure ratio across the preswirl ring. Since the FPDS leakage rate is higher than that of the honeycomb and labyrinth seals, the preswirl values for the FPDS are larger for the medium and high preswirl ring tests.

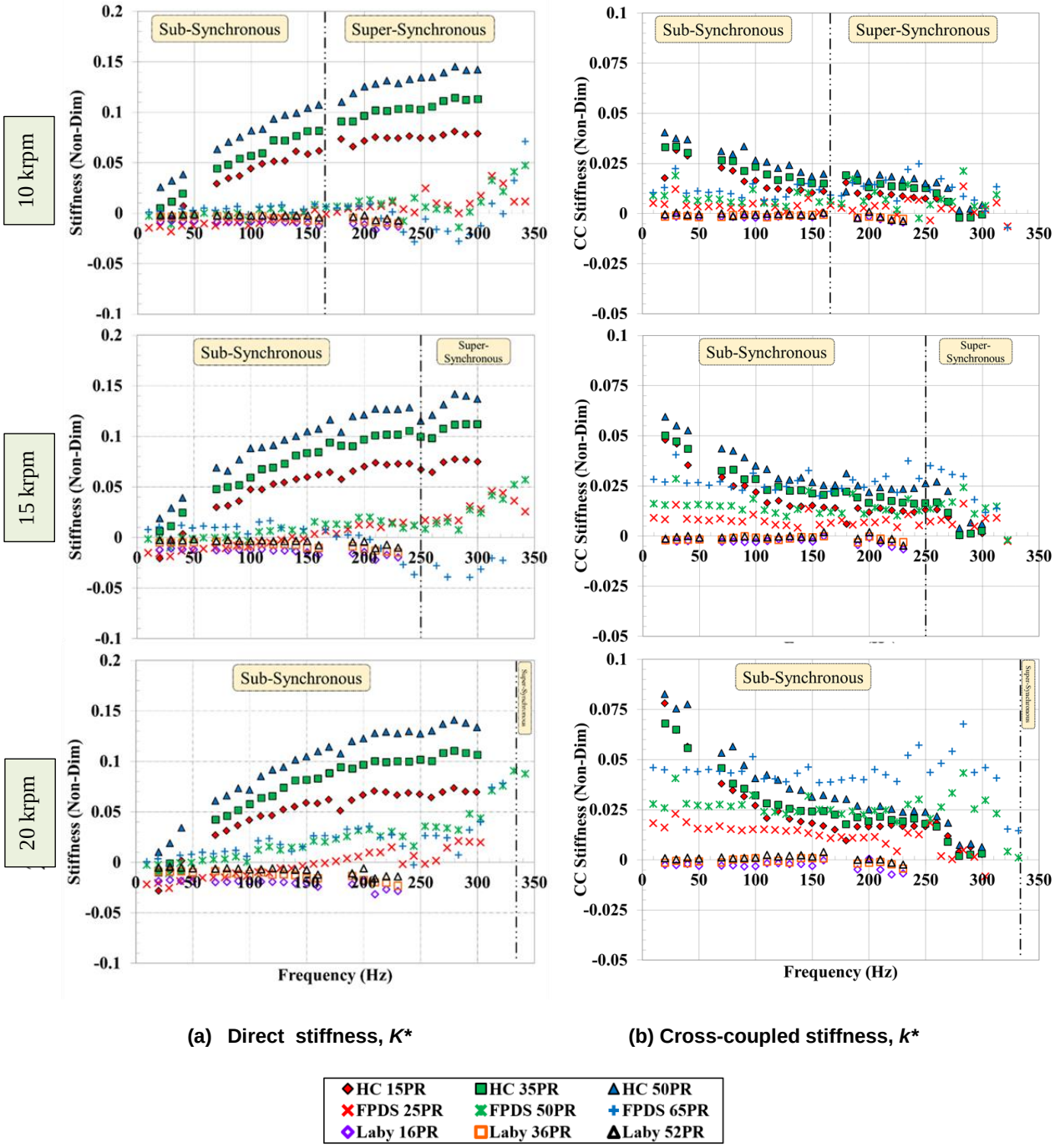

Figure 14 (Normalized) Direct stiffness (*K) and cross-coupled stiffness (*k**) coefficients versus excitation frequency for pocket damper seal (FPDS), honeycomb seal (HC), and labyrinth seal (LS). Multiple pressure ratios PR = 15% – 65%, three rotor speeds (10, 15, 20 krpm), and a low inlet pre-swirl condition (α < 0.1) for the three seals.**

Figure 15 shows the direct (C^*) and effective damping ($C_{eff}^* = C^* - k^*/(\omega/\Omega)$) coefficients versus excitation frequency for tests with the low pre-swirl ring (with FPDS), various pressure ratios (*PR*), and three shaft speeds. Note the difference in vertical scales for the C^* and C_{eff}^* force coefficients.

As expected, the labyrinth seal offers negligible damping coefficients, hence merits no further discussion. The HC offers the largest damping (C^*) at low excitation frequencies and is not affected by the pressure ratio (*PR*) or even shaft speed. On the other hand, the FPDS offers a nearly constant C^* for excitation frequencies below shaft speed ($\omega < \Omega$), though modestly increasing as the *PR* increases. The direct damping for the HC decreases steadily with excitation frequency, and thus becomes lower than the damping coefficient for the FPDS at $\omega > \Omega$. This difference proves crucial for excitation at synchronous shaft speed or larger frequencies.

In spite that the HC offers a large damping coefficient at low frequencies, its $C_{eff}^* < 0$ since the cross-coupled stiffness (k) is significant.

The same observation holds for the FPDS. However, for high frequencies ($\omega >$ 150 Hz), the FPDS offers a larger effective damping coefficient (C_{eff}^*) than the HC does. Note though the HC evidences a higher magnitude C_{eff}^* just above the cross-over frequency (ω_{co} making $C_{eff}^* = 0$); for example, see data at ~ 100 Hz.

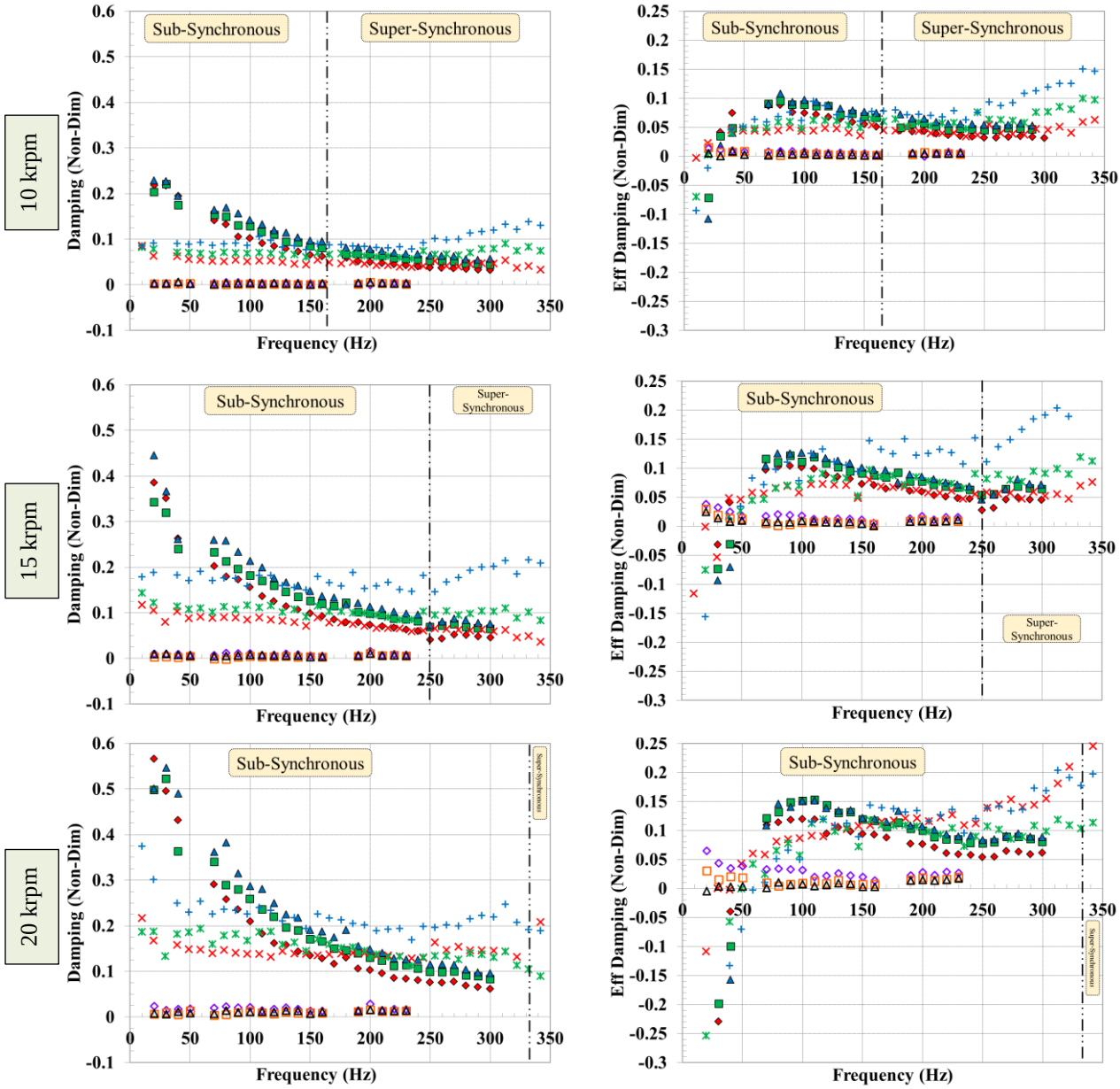

(a) Direct damping, C^* **(b) Effective damping, C^*_{eff}**

Figure 15 (Normalized) Direct damping (C^*) and effective damping (C^*_{eff}) coefficients versus frequency for pocket damper seal (FPDS), honeycomb seal (HC), and labyrinth seal (LS). Multiple pressure ratios PR = 15% – 65%, three rotor speeds (10, 15, 20 krpm), and a low inlet pre-swirl condition (α < 0.1) for the three seals.

For both the FPDS and HC operating at three rotor speeds, Figure 16 depicts the cross-over frequency (ω_{co}) versus inlet pre-swirl ratio as obtained from the effective damping results. The FPDS shows a slightly lower ω_{co} (~20%) for the low inlet pre-swirl condition. Note ω_{co} increases with the inlet pre-swirl ratio, with the FPDS showing a higher rate of growth than the HCl. For operation at the highest shaft speed, the cross-over frequency for the FPDS is larger than the ω_{co} for the HC.

While damper seals are typically installed with a swirl mitigation device (either swirl brakes or shunt injection), the current experimental results highlight the influence of inlet pre-swirl on raising the cross-over frequency (as the cross-coupled stiffness k increases), and the importance of reducing inlet pre-swirl.

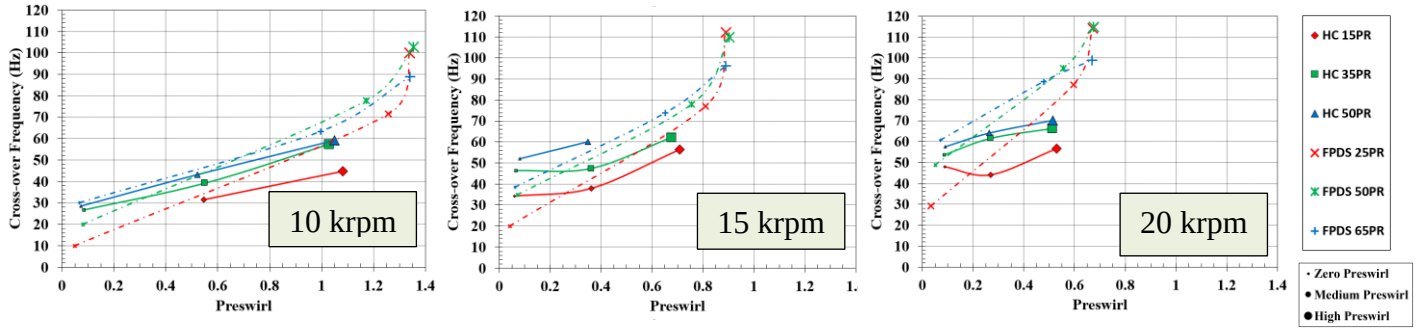

Figure 16 Cross-over frequency versus (ω_{co}) inlet pre-swirl ratio (α) for FPDS and honeycomb seal (HC) [5] . Multiple pressure ratios *PR* = 15% – 65% and three rotor speeds (10, 15, 20 krpm). Inlet pre-swirl obtained with low, medium and high pre-swirl rings.

A comparison of mass flow rates is also appropriate. To this end, a flow coefficient ($\bar{\phi}$) is most appropriate and defined as [4]

$$\bar{\phi} = \frac{\dot{m}}{\pi \cdot C_r \cdot D} \sqrt{\frac{R_g \cdot T_{in}}{2 \cdot \left(P_{in}^2 - P_{out}^2\right)}} \tag{7}$$

For the three seals considered; HC, FPDS and LS, Figure 17 depicts the flow coefficient ($\bar{\phi}$) versus pressure ratio (*PR).* Above the T_{in} mean magnitude is 285.3 K (12 ºC or 54 ºF). The data shown corresponds to a mean value from tests conducted at three shaft speeds (10, 15 and 20 krpm). Note the flow coefficient slightly increases as the pressure ratio rises. The FPDS leaks more than the LS does, 10 % higher; whereas the HC leaks the least, ~ 15% less than the LS does. These results are consistent with the FPDS having a cavity surface area larger than that of the other two seals, that is γ= cavity surface area/FPDS inner surface area = 0.89.

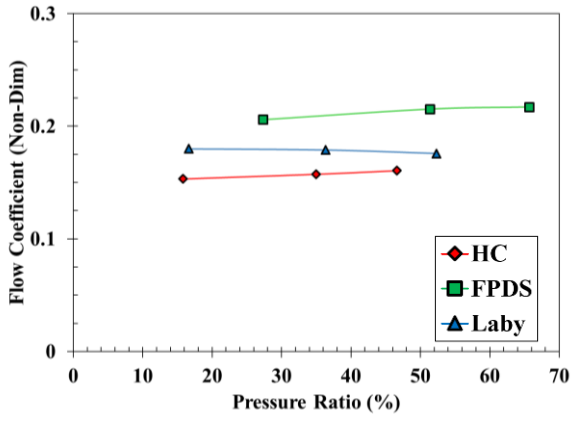

Figure 17 Flow coefficient ($\bar{\phi}$) vs. pressure ratio for honeycomb seal (HC) [21], fully partitioned pocket damper seal (FPDS), and labyrinth seal (LS) [34]. Average from operation at three shaft speeds (10, 15, 20 krpm). Seals with medium inlet-swirl ring.

While it may be argued that the FPDS, like labyrinth seals, could be designed with a tighter clearance than that in a honeycomb seal, it is expected that the honeycomb seal would still provide a comparable or better leakage performance. In terms of manufacturing, the original honeycomb seal in Ref. [21] would be expensive to make, hence giving an advantage to the FPDS. However, a hole-pattern damper seal can produce similar benefits as a honeycomb seal does while being simpler to manufacture when compared to the FPDS (less material removal). Furthermore, manufacturability does not differ between the FPDS and these textured surface seals if plunge EDM (electro-discharge machining) is used to create the honeycomb pattern or a simple right-angle drill to create a hole-pattern seal.

As per force coefficients, the direct stiffness coefficient (*K*) is the main difference between the test honeycomb seal and the FPDS, see Figure 14. The pocket damper seal produces a minute *K* compared to that in the HC. At a high frequency ($\omega > \Omega$), the FPDS produces an effective damping coefficient similar or larger in magnitude than the C_{eff} the honeycomb seal shows. Depending on the specific application, a HC may be used to improve stability by increasing the compressor natural frequency (i.e. increase the onset speed of instability) and by increasing the damping ratio of the vibration mode of interest. For example, in a back-to-back compressor, this seal can convert the compressor into a "3-bearing" machine and the calculated stability improvement follows as much from the stiffness increase as from the damping increase. On the other hand, the FPDS could be used to improve the system damping ratio without significantly affecting the rotor-bearing system natural frequencies. In this manner, the pocket damper seal would preserve the placement of the critical speeds and their separation margins [35].

Comparison of predicted (CFD and BFM) force coefficients and experimental force coefficients

As detailed earlier, the CFD model for prediction of the FPDS dynamic force coefficients employs fourteen excitation frequencies, $\{\omega_j\} = 2\pi$ {25 Hz, 50 Hz… 350 Hz} ($N = 14$). The whirl period to complete a rotor elliptic orbit is $T = 0.04$ s. The number of time steps per rotor whirl orbit is 500 (0.08 ms per step). The CFD analysis employs the computing resources from the High Performance Research Computing (HPRC) at TAMU and schedules up to 40 cores per the three dimensional unsteady state flow case. It takes ~ 46 h CPU time to compute one full period of rotor whirl motion. It takes about 4T for the unsteady flow analysis to converge when the difference in predicted force coefficients, obtained from the third period and fourth period, is less than 4%.

For tests with a *PR* = 0.65 (P_{in}= 70 bar) and a zero inlet pre-swirl ratio, Figure 18 shows the test identified, CFD predicted and BFM predicted direct stiffness (K), cross-coupled dynamic stiffness (k), direct damping (C), and effective damping ($C_{eff} = C - k/\omega$) versus the excitation frequency (ω) for the FPDS operating at three rotor speeds (Ω = 10 krpm, 15 krpm and 20 krpm). The error bars on the test data represent the variability of the two excitation directions (X and Y).

The test direct stiffness K varies slightly with an increase in frequency ω, in particular at low frequency (ω < 200 Hz) for rotor speed Ω = 10 krpm and 15 krpm. While for Ω = 20 krpm, the test K shows a growth as ω increases. The CFD predicted K grows consistently with an increase in ω, having a larger magnitude than the test data for all the three rotor speeds. The BFM prediction of direct stiffness K is slighter greater than the test data for the two rotor speeds Ω = 10 krpm and 15 krpm. Whereas the BFM K is smaller than the test value when ω > 100 Hz for rotor speed Ω = 20 krpm. The test cross-coupled dynamic stiffness k, independent of the whirl frequency ω, enlarges with an increase in Ω. The variability of test k turns large for ω > 280 Hz. The CFD and BFM predicted k agree with the test data for Ω = 10 krpm. For rotor speed Ω = 15 krpm and 20 krpm, the CFD and BFM predictions are larger and smaller than the test results respectively.

The test direct damping coefficient C decreases slightly with an increase in frequency ω for ω < 250 Hz, and then increases with the growing ω. Neither the CFD predicted C nor the BFM prediction captures this variation trend versus frequency ω as the test data. But at low frequencies (ω < 250 Hz), the CFD C matches well with the test data, in particular for Ω = 20 krpm. The BFM predicted C, increasing with ω, is larger than the test C. For instance, the BFM predicted C is ~ 20% greater than the test data for Ω = 10 krpm (ω/Ω = 1). The test derived effective damping coefficient C_{eff} decreases continuously with an increase in Ω. The CFD predicted and BFM predicted C_{eff} is lower and greater than the test data respectively, mainly due to their deviations in direct damping C with the test results.

For tests with a *PR* = 0.50 (P_{in}= 70 bar) and a zero inlet pre-swirl ratio, Figure 19 displays the test derived, CFD predicted and BFM predicted direct dynamic stiffness (K), cross-coupled dynamic stiffness (k), direct damping (C), and effective damping (C_{eff}) for the FPDS operating at three rotor speeds (Ω = 10 krpm, 15 krpm and 20 krpm). The test K grows with an increase in frequency ω. K also increases with an increase in the rotor speed Ω. In comparison to the test data for PR = 0.65, the test K drops at low excitation frequency (ω < 150 Hz). The CFD predicted K show similar increasing trends versus ω, though with a larger magnitude than all the test results for the three rotor speeds. The BFM predicted K is larger than the test results at low ω (< 150 Hz) for the three rotor speeds. At higher ω (> 150 Hz), the BFM prediction agrees with test K when Ω = 15 krpm. The test derived cross-coupled dynamic stiffness k increases with the increase in Ω. The CFD prediction of k is higher than the test data, and decreases gradually vs. ω. The BFM predicted k is close to the test results for Ω = 10 krpm and Ω = 15 krpm. The test direct damping coefficient C decreases with an increase in frequency ω. The CFD predicted C agrees well with the test data, capturing the decreasing trend of C versus ω. The BFM C, growing slightly with ω, deviates with the test data with a larger magnitude. Similar to the test results for PR = 0.65, the test effective damping coefficient C_{eff} decreases continuously with an increase in Ω. The CFD predicted C_{eff} is smaller than the test C_{eff}, for the CFD predicted k is larger than test k. The BFM prediction of C_{eff} is higher than the test result, due to the large BFM predicted C.

For tests with a *PR* = 0.25 (P_{in}= 70 bar) and a zero inlet pre-swirl ratio, Figure 20 shows the test derived, CFD and BFM predicted force coefficients for the FPDS vs. frequency. Note the test data for the rotor speed Ω = 20 krpm is not available due to a rotor-bearing system instability. In comparison to the test results for PR = 0.5, the test direct stiffness K for PR = 0.25 further drops into negative at low frequency (ω < 150 Hz). While the CFD predicted and BFM predicted K are positive for all the excitation frequency. The test cross-coupled stiffness k enlarges from Ω = 10 krpm to Ω = 15 krpm. The CFD predicted k is larger than the test data, while the BFM prediction agrees with the test k. The CFD predicted direct damping C matches well with the test C for Ω = 10 krpm and Ω = 15 krpm. Since the CFD k is greater than the test data, the CFD predicted effective damping C_{eff} is smaller than the test C_{eff}. The BFM predicted C_{eff} is slightly higher than the test C_{eff} at the low excitation frequency (ω < 100 Hz).

Figures 21 through 23 present the comparison of the FPDS force coefficients between BFM predictions and the experimental data obtained with the medium preswirl ring for three pressure ratios (PR=0.65, 0.5, 0.25) and at shaft speeds (10, 15, 20 krpm). These tests correspond to relatively high preswirl conditions (α=1.3 - 0.83) listed in Table 2. For PR=0.65, the BFM produces a close estimation of the seal direct stiffness (K) at low frequencies and overestimates (<30%) the cross-coupling and direct damping (k, C) coefficients. As a result the BFM overestimates the cross-over frequency (ω_{co}) by ~25%, but the overall effective damping (C_{eff}) magnitudes correlate well with the experimental coefficients. For PR=0.5, the BFM K is higher than the experimental results at low frequencies. The predicted k matches well the experimental results for 10 and 15 krpm, while at 20 krpm the BFM over predicts this coefficient by ~30%. With predicted C that are slightly higher (10-20%) than those obtained from the experimental results, the resultant ω_{co} and C_{eff} show good correlation between experiments and predictions at frequencies near ω_{co} for 10 and 15 krpm. For the 20 krpm case, the results look similar to those reported for PR=0.65; there is an overall good match but the BFM overpredicts ω_{co}. Lastly, for PR=0.25, the BFM

predicts positive direct stiffnesses while the experiments show negative values ($K<0$) at low frequencies. The BFM cross-coupled stiffness (k) predictions correlate well with the experimental results. The BFM predicted damping coefficient (C) are relatively constant with frequency, whereas the experimental results show C's that linearly decay with frequency. However, the overall difference at low frequencies (<160 Hz) is relative small (~ 10%), thus yielding good estimates of ω_{to} and C_{eff} within that frequency range.

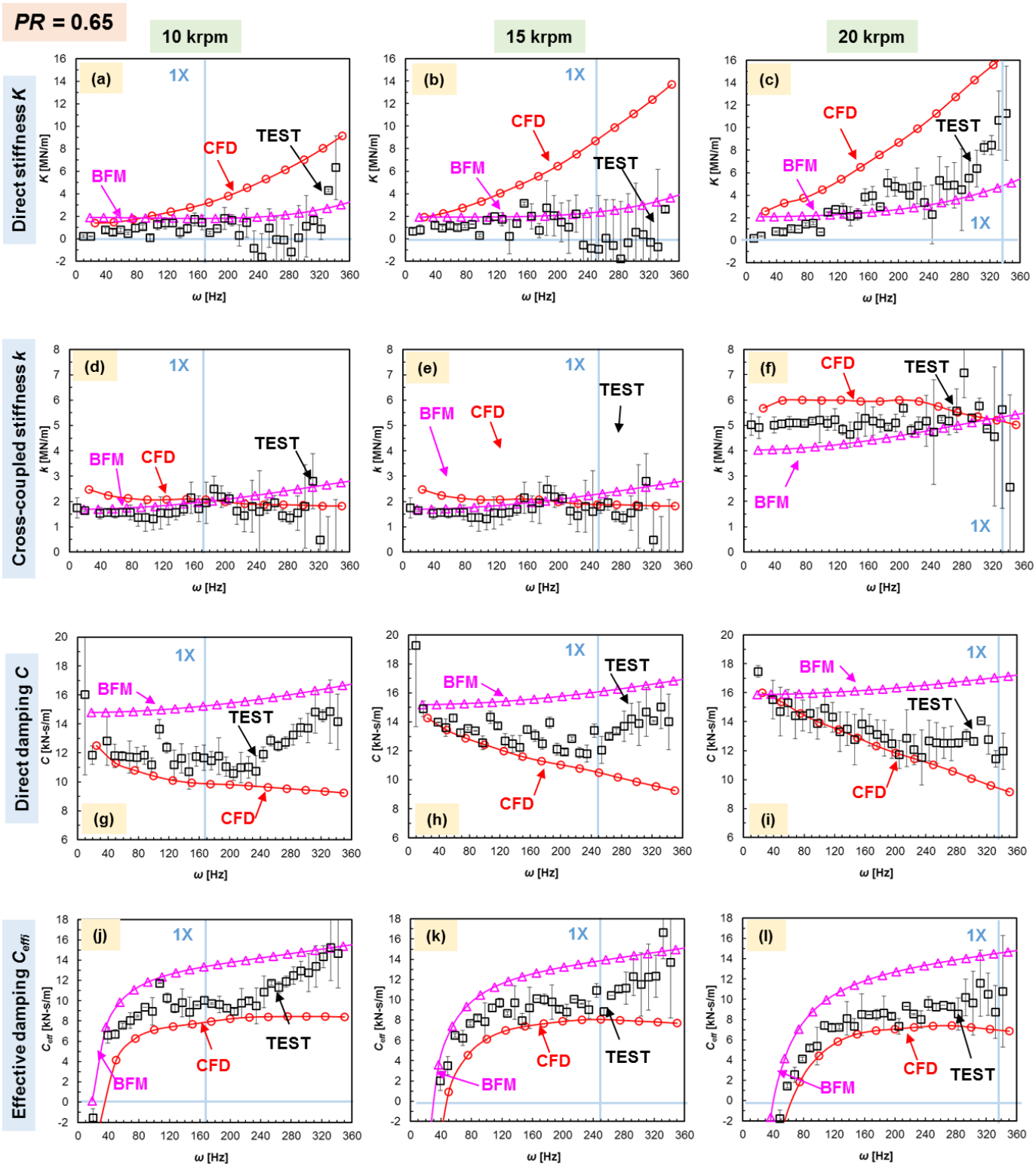

Figure 18 FPDS: test, CFD and BFM predicted force coefficients (K, k, C, C_{eff}) vs. frequency (ω) for P_{in} = 70 bar, PR = 0.65. Shaft speeds: 10, 15 and 20 krpm (½ΩD = 60 to 120 m/s), zero inlet pre-swirl condition.

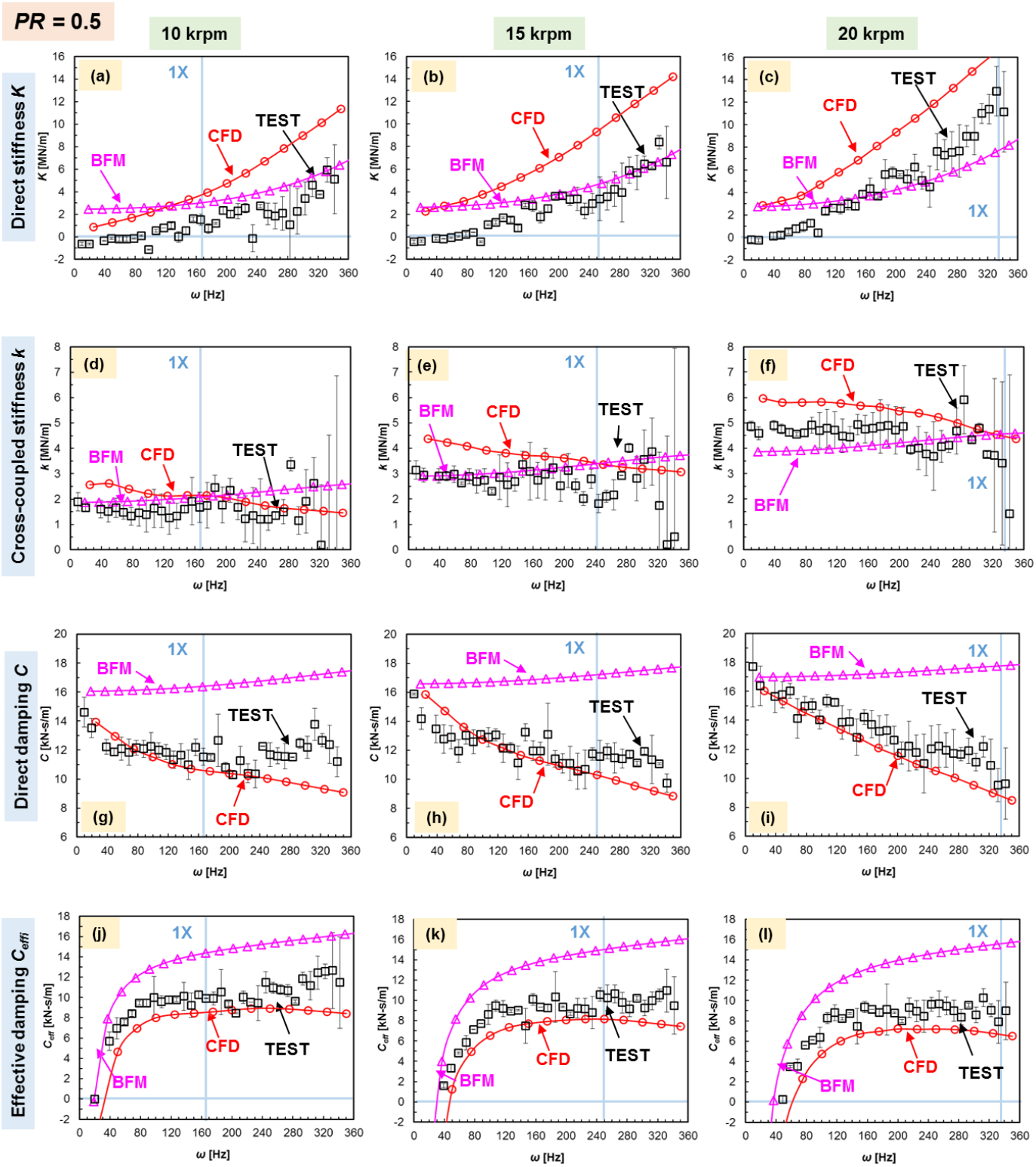

Figure 19 FPDS: test, CFD and BFM predicted force coefficients (*K, k, C, C_{eff}*) vs. frequency (ω) for P_{in} = 70 bar, *PR* = 0.5. Shaft speeds: 10, 15 and 20 krpm (½Ω*D* = 60 to 120 m/s), zero inlet pre-swirl conditions.

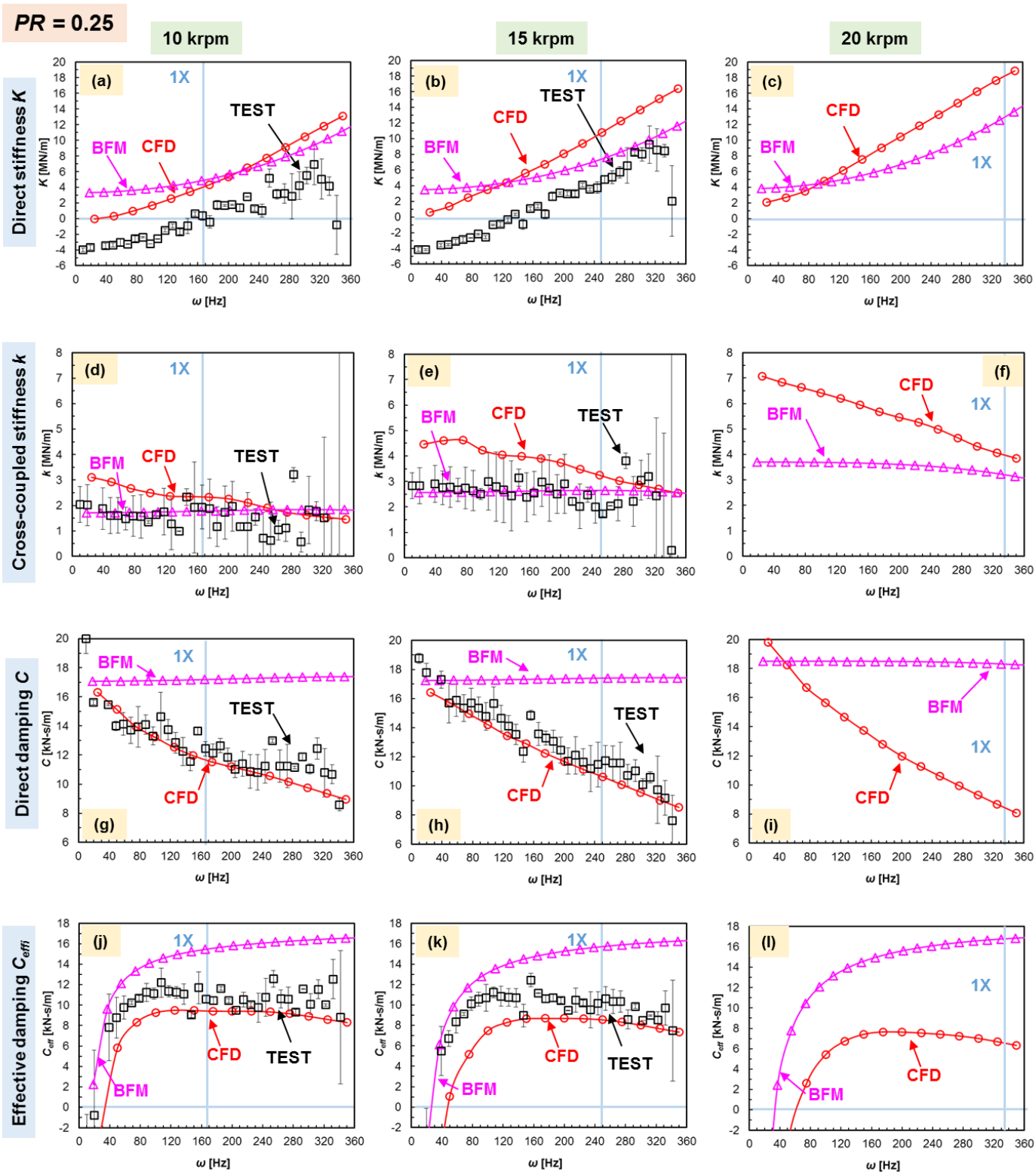

Figure 20 FPDS: test, CFD and BFM predicted force coefficients (*K*, *k*, *C*, C_{eff}) vs. frequency (ω) for P_{in} = 70 bar, *PR* = 0.25. Shaft speeds: 10, 15 and 20 krpm (½Ω*D* = 60 to 120 m/s), zero inlet pre-swirl conditions.

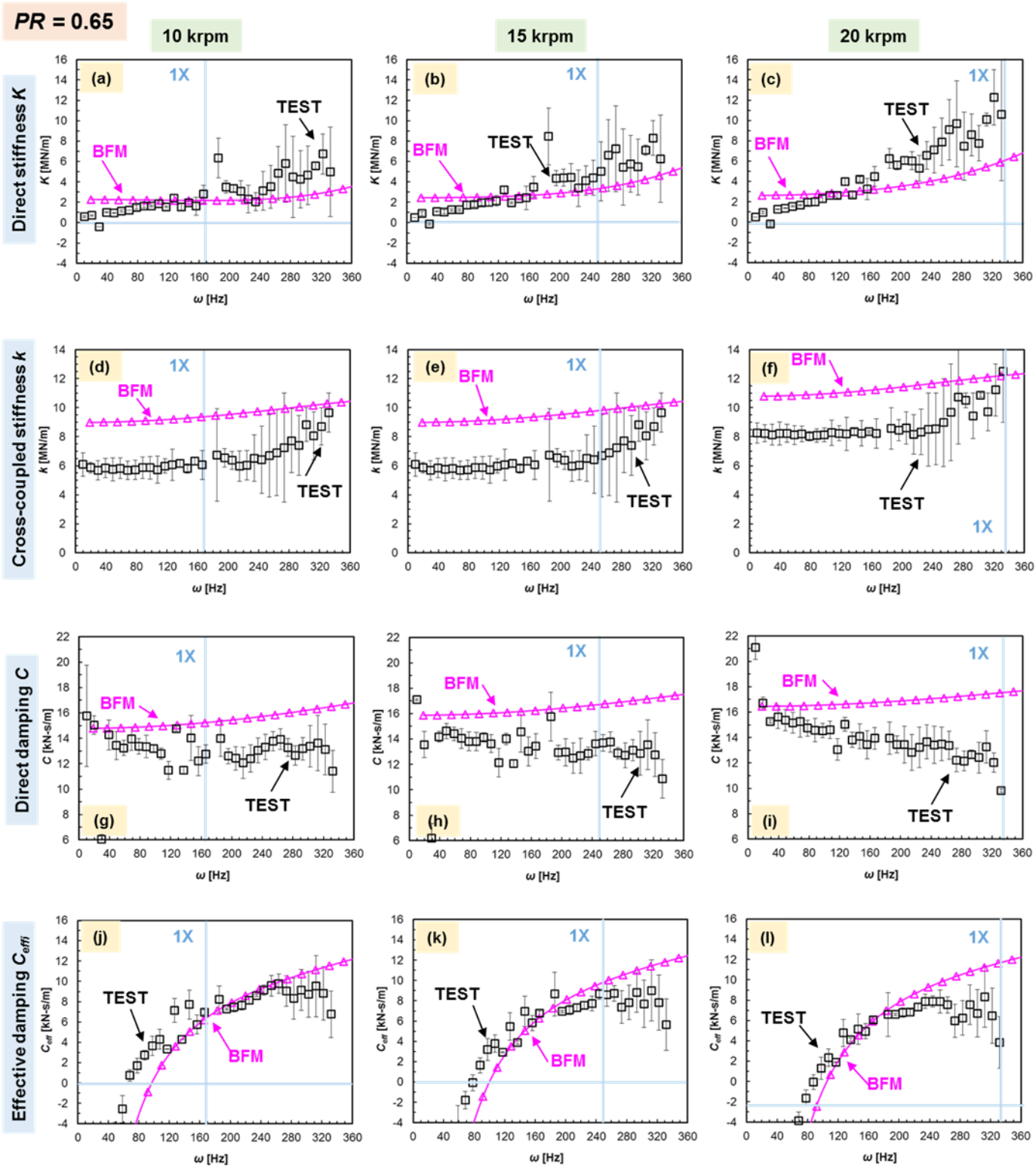

Figure 21 FPDS: test and BFM predicted force coefficients (*K*, *k*, *C*, C_{eff}) vs. frequency (ω) for P_{in} = 70 bar, *PR* = 0.65. Shaft speeds: 10, 15 and 20 krpm (½Ω*D* = 60 to 120 m/s), medium inlet pre-swirl condition.

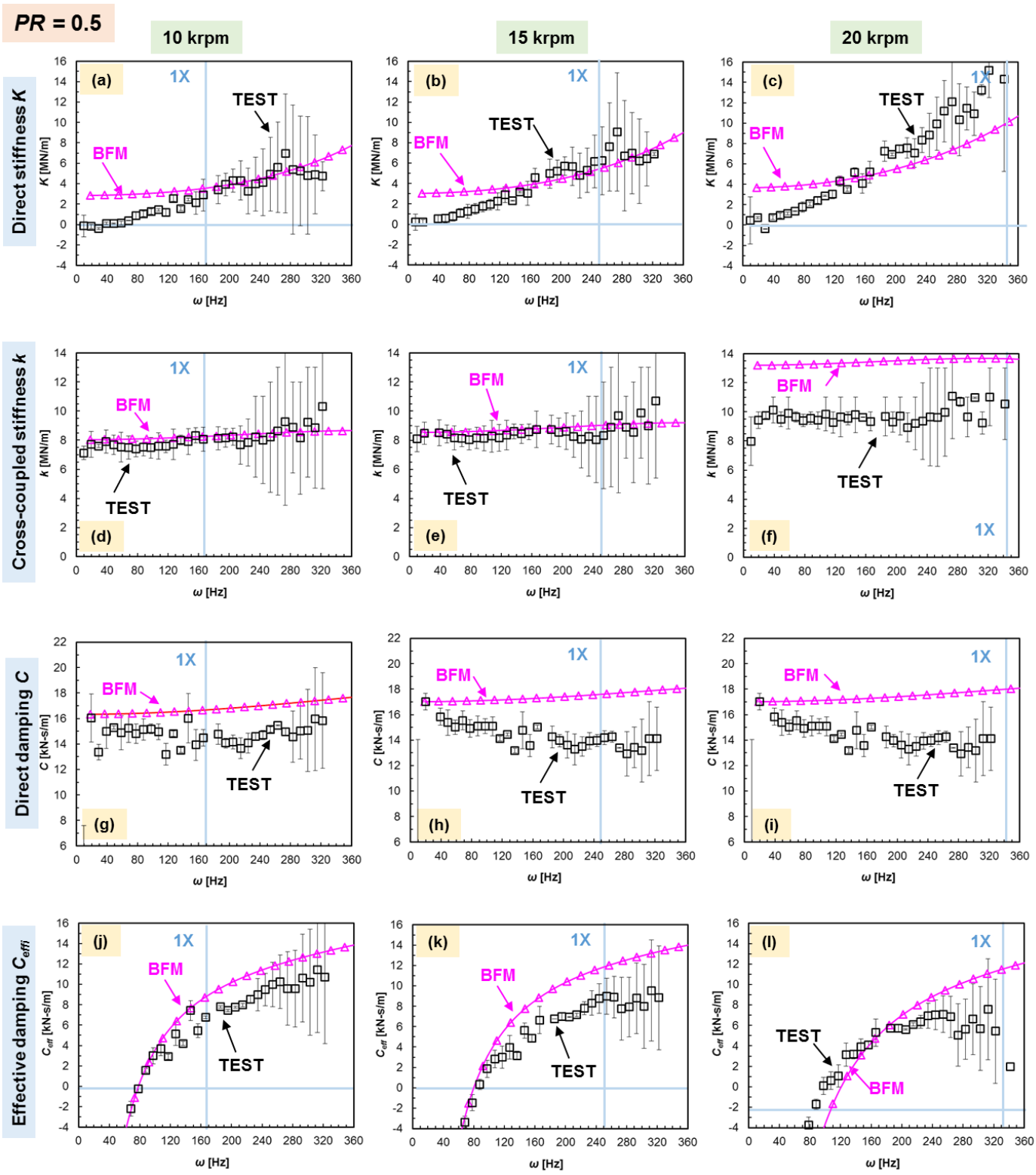

Figure 22 FPDS: test and BFM predicted force coefficients (*K*, *k*, *C*, C_{eff}) vs. frequency (ω) for P_{in} = 70 bar, *PR* = 0.5. Shaft speeds: 10, 15 and 20 krpm (½Ω*D* = 60 to 120 m/s), medium inlet pre-swirl condition.

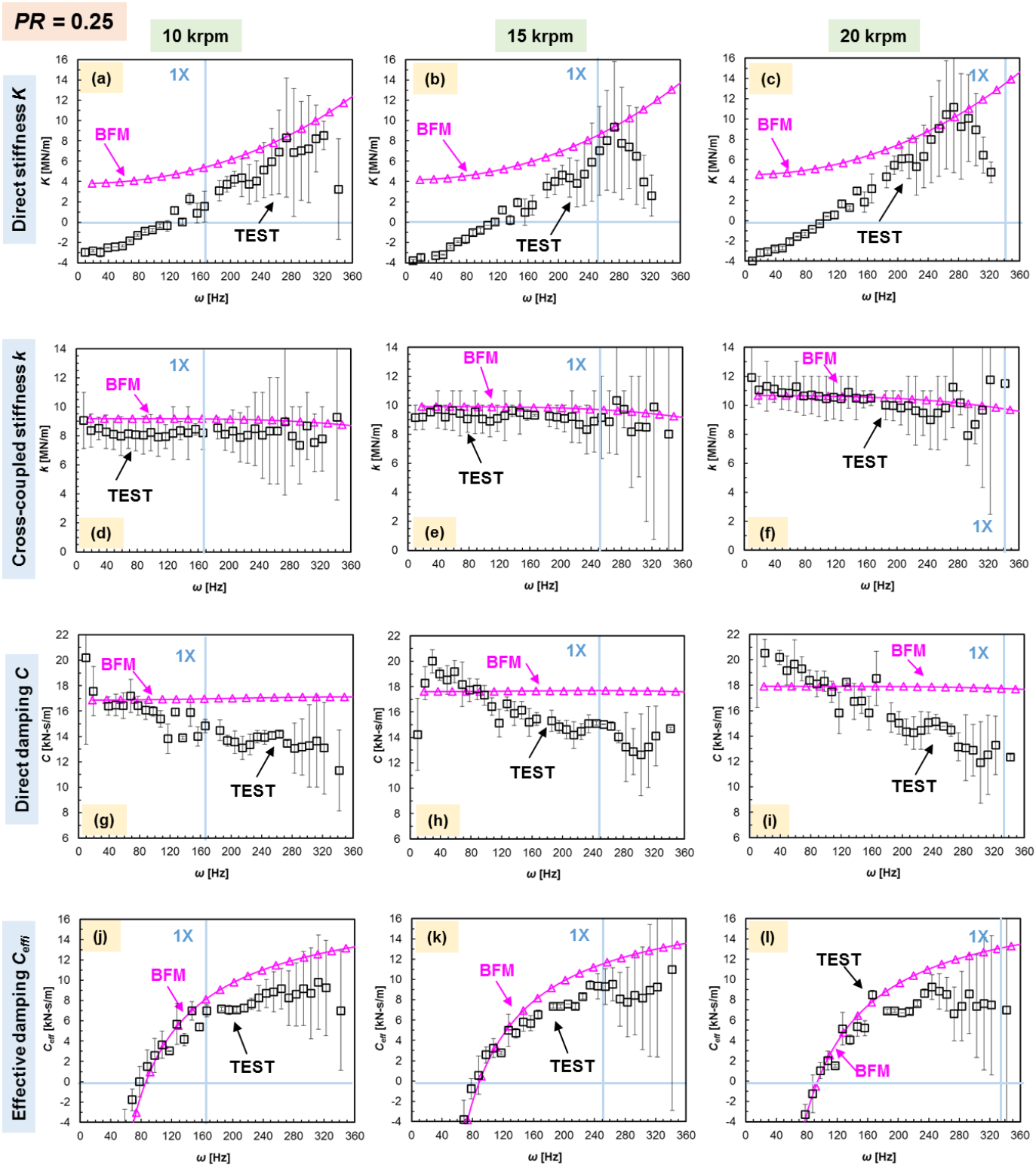

Figure 23 FPDS: test and BFM predicted force coefficients (*K*, *k*, *C*, C_{eff}) vs. frequency (ω) for P_{in} = 70 bar, *PR* = 0.25. Shaft speeds: 10, 15 and 20 krpm (½Ω*D* = 60 to 120 m/s), medium inlet pre-swirl condition.

CONCLUSIONS

Fully partitioned damper seals (FPDS) represent an alternative design to textured seals (HC and hole-pattern) for increasing stability margin of centrifugal compressors. Multiple numerical and experimental investigations on textured seals have produced a significant amount of experimental data together with benchmarked predicted models. On the other hand, there is not a comprehensive data set of experimental force coefficients for FPDS that would allow for a fair comparison against textured seals and an exhaustive benchmarking

against predictive models. This work aims at providing such data set by identifying the force coefficients of a FPDS in the same test rig used to generate most of the data available for textured seals, and by comparing the experimental results against CFD and a bulk-flow model predictions. Hence, experimental dynamic force coefficients and leakage are presented for a FPDS operating with air supplied at P_{in}=70 bar, thee pressure ratios $PR=P_{out}/P_{in}$ =35%, 50%, 65%, shaft speeds (10, 15 and 20 krpm: max rotor surface speed of 120 m/s), and inlet circumferential flow pre-swirl ratios ($\alpha = 0.2$-1.2). The experimental results allow comparisons against published test data for a honeycomb seal (HC) and a labyrinth seal (LS), both similar in size and clearance as the FPDS, and operating at similar pressure and shaft speed conditions. Predictions from both a bulk-flow model and a CFD model compared vis-à-vis the experimental results for the FPDS attest to the accuracy (or lack thereof) of the current numerical tools. The experimental results will aid in the engineered design of pocket damper seals.

The FPDS direct stiffness coefficients are negative or very small (-4 MN/m < K < 4MN/m) at low frequencies and decrease as the pressure ratio increases. Unlike in the case of textured seals, the K magnitudes are expected to have a minimal impact on the vibration mode shapes and natural frequencies of a typical compressor rotor-bearing system. In terms of cross-coupling stiffness coefficients (k), the experiments yielded frequency-independent results that increase in magnitude as the rotor speed and pre-swirl increases, and decrease as the pressure ratio increases. The overall magnitudes at low frequencies (<100) are lower than those published for HC, and become comparable at higher frequencies.

The FPDS direct damping decreases with frequency and its overall magnitude decreases as the pressure ratio increases. The FPDS exhibits less damping than the HC at low excitation frequencies. Effective damping magnitudes are negative at low excitation frequencies, which is a characteristic behavior of damper seals. The measured C_{eff} increases in magnitude with increasing rotor speed and inlet circumferential flow pre-swirl. The effective damping increases with increasing synchronous excitation frequency. The cross-over frequencies improve greatly when transitioning from a high to a low inlet pre-swirl condition, from ~100 Hz to ~50 Hz. The FPDS and HC have similar effective damping coefficients. At low pre-swirls, the FPDS has favorable cross-over frequencies when compared to the HC. While the HC has lower cross-over frequency when inlet pre-swirl increases. Unlike textured seals, the FPDS produces low cross-coupled damping coefficients that do not significantly affect the seal effective stiffness (~ direct stiffness). In HC, cross-coupled damping increases with frequency and can be large enough to significantly lower the rotor-bearing system natural frequency.

Besides the experimental research, the CFD and BFM provide two numerical approaches investigating the dynamic forced performance for FPDS. For operation with a low inlet swirl ($\alpha \sim 0$), the CFD predicted direct damping coefficient (C) agrees well with the test data and captures the decreasing trend of C as the excitation frequency grows. The CFD direct stiffness (K) shows a larger magnitude than the test results, hence it needs to improve. Besides the leakage and dynamic force coefficients, the CFD results also provide high resolution pressure contours, velocity vectors and streamlines inside the seal (not shown in the lecture) that aid to understand (via visual art) the complex flow patterns in a FPDS. The BFM model predicted cross-coupled stiffness k agrees with the test data, while showing a large discrepancy on the predicted direct damping C against the test results. The BFM is a fast tool to predict the seal dynamic force coefficients, hence its wide applicability in routine engineering tasks. The concerted exercise of both numerical methods, CFD and BFM, can be effectively applied in the design and optimization of damper seals, in particular FPDS.

Lastly, the FPDS leaks 20% - 25% more than the HC does as the pressure ratio increases. Besides manufacturing considerations, the FPDS may be a better alternative to a textured damper seal (e.g. a honeycomb seal) when the centering stiffness, typical of textured seals, may increase the compressor critical speed and decrease the separation margin respect to the running speed, and which could place the compressor out of API compliance. In these cases, the FPDS represents a better alternative for improving system stability.

NOMENCLATURE

C, c	Direct and cross-coupled damping coefficients [Ns/m]
C_{eff}	Effective damping coefficient [Ns/m], $C_{eff} = C - k/\omega$
C_r	Seal radial clearance [m]
D	$2R$. Rotor diameter [m]
F_X, F_Y	Seal reaction force components (radial and tangential) [N]
H, h	Direct and cross-coupled dynamic stiffnesses [N/m]
K, k	Direct and cross-coupled stiffness coefficients [N/m]
K_{eff}	Effective stiffness coefficient [N/m], $K_{eff} = K + c\omega$
$\dot{m}$	Leakage (mass flow rate) [kg/s]
P	Static pressure [Pa]
P_{in}, P_{out}	Supply (inlet) and discharge (exit) pressures [Pa]
PR	Pressure ratio, $PR = P_{out}/P_{in}$
R	Rotor radius [m]
R_g	Ideal gas constant [J/(kg·K)], R_g = 287.15 J/(kg·K) for air
T_{in}	Temperature of gas [K].
X, Y	Rotor displacements in radial and tangential directions [m]
α	Swirl ratio, α = circumferential velocity/rotor surface speed

ρ	Density, [kg/m^3]
$\bar{\phi}$	Flow factor, $\bar{\phi} = \dfrac{\dot{m}}{\pi \cdot C_r \cdot D} \sqrt{\dfrac{R_g \cdot T_{in}}{2 \cdot \left(P_{in}^2 - P_{out}^2\right)}}$
ω	Whirl frequency [rad/s]
ω_{oc}	Cross-over frequency [rad/s]
Ω	Rotor angular velocity [rad/s]

Abbreviations

BFM	Bulk flow model
CFD	Computational Fluid Dynamics
HC	Honeycomb seal
FPDS	Fully partitioned pocket damper seal
HPOTP	High pressure oxygen turbopump
LS	Labyrinth seal
PDS	Pocket damper seal
SSME	Space shuttle main engine

REFERENCES

[1] Fowlie, D. W., and Miles, D. D., 1975, "Vibration Problems with High Pressure Centrifugal Compressors," ASME Paper No. 75-PET-28.

[2] Highest Pressure Gas Injection Centrifugal Compressors," Proceedings of the Eighth Annual Offshore Technology Conference, Houston, TX, pp. 3-6.

[3] Kocur, J., Cloud, C. H., Pettinato, B, 2018, "Predicting, Understanding and Avoiding the Ekofisk Rotor Instability Forty Years Later," Proceedings of the 47th Turbomachinery and 34th Pump Symposium, Turbomachinery Laboratory, Texas A&M Engineering Experiment Station, URI: http://hdl.handle.net/1969.1/174995.

[4] Childs, D. W., 2013, *Turbomachinery Rotordynamics with Case Studies*, Minter Spring, College Station, TX.

[5] Zhang, M., and Childs, D. W., 2020, "A Study for Rotordynamic and Leakage Characteristics of a Long-Honeycomb Seal with Two-Phase, Mainly Air Mixtures," ASME. J. Eng. Gas Turbines Power, **142**(1), p. 011021

[6] Childs, D. W., 1993, *Turbomachinery Rotordynamics: Phenomena, Modeling, and Analysis*, Wiley, New York.

[7] Alford, J. S., 1965, "Protecting Turbomachinery from Self-Excited Rotor Whirl," Journal of Engineering for Power, **87**(4), pp. 333-343.

[8] Benckert, H., and Wachter, J., 1980, "Flow Induced Spring Coefficients of Labyrinth Seals for Application in Rotor Dynamics," Workshop on Rotordynamic Instability Problems in High-Performance Turbomachinery, Texas A&M University, College Station, TX, May 12–14, pp. 189–212.

[9] Von Pragenau, G. L., 1982, "Damping Seals for Turbomachinery," NASA Technical Report No. NASA-TP-1987, Available on https://ntrs.nasa.gov/search.jsp?R=19820012309.

[10] Childs, D., Elrod, D., and Hale, K., 1989, "Annular Honeycomb Seals: Test Results for Leakage and Rotordynamic Coefficients; Comparisons to Labyrinth and Smooth Configurations," ASME. J. Tribol., **111**(2), pp. 293–300

[11] Childs, D., Elrod, D., and Ramsey, C., 1990, "Annular Honeycomb Seals: Additional Test Results for Leakage and Rotordynamic Coefficients," Proceedings of IFTOMM Third International Conference on Rotordynamics, Lyon, France.

[12] Vance, J. M., and Shultz, R. R., 1993, "A New Damper Seal for Turbomachinery," Proceedings of 14th Vibration and Noise Conference, Sept. 19–22, Albuquerque, NM, pp. 139–148.

[13] Vance, J. M., and Li, J., 1996, "Test Results of a New Damper Seal for Vibration Reduction in Turbomachinery," ASME J. Eng. Gas Turbines Power, **118**(4), pp. 843-846.

[14] Ertas, B. H., Delgado, A., and Vannini, G., 2012, "Rotordynamic Force Coefficients for Three Types of Annular Gas Seals With Inlet Pre-swirl and High Differential Pressure Ratio," ASME J. Eng. Gas Turb. Power, **134**(4), pp. 511-522.

[15] Vannini, G., Mazzali, C., and Underbakke, H., 2016, "Rotordynamic Computational and Experimental Characterization of a Convergent Honeycomb Seal Tested With Negative Pre-Swirl, High Pressure With Static Eccentricity and Angular Misalignment," ASME Paper No. GT2016-56615.

[16] Vance, J. M., Murphy, B., and Zeidan, F., 2010, *Machinery vibration and rotordynamics*, Wiley, New York.

[17] Vannarsdall, M. L., 2011, "Measured results for a new hole-pattern annular gas seal incorporating larger diameter holes,

comparisons to results for a traditional hole-pattern seal and predictions," Master thesis, Texas A&M University, College Station, TX.

[18] Li, J., San Andrés, L., and Vance, J., 1999, "A Bulk-Flow Analysis of Multiple-Pocket Gas Damper Seals," ASME J. Eng. Gas Turbines Power, **121**(2), pp. 355-363.

[19] Li, J., 1995, "The effect of a new damper seal on rotordynamics", Master thesis, Texas A&M University, College Station, TX.

[20] Li, J., Kushner, F., and DeChoudhury, P., 2000, "Gas Damper Seal Test Results, Theoretical Correlation, And Applications In Design Of High-Pressure Compressors," Proceedings of the 29th Turbomachinery and Pump Symposium, Texas A&M University. Turbomachinery Laboratories. URI: http://hdl .handle .net /1969.1/163353.

[21] Sprowl, T. B., 2003, "A Study of the Effects of Inlet Pre-swirl on the Dynamic Coefficients of a Straight-bore Honeycomb Gas Damper Seal," Master thesis, Texas A&M University, College Station, TX.

[22] Ertas, B. H., 2005, "Rotordynamic force coefficients of pocket damper seals," Ph.D. thesis, Texas A&M University, College Station, TX.

[23] Ertas, B., Gamal, A., and Vance, J., 2006, "Rotordynamic Force Coefficients of Pocket Damper Seals," ASME J. Turbomach., **128**(4), pp. 725-737.

[24] Brown, P. D., and Childs, D. W., 2012, "Measurement Versus Predictions of Rotordynamic Coefficients of a Hole-Pattern Gas Seal With Negative Pre-swirl," ASME J. Eng. Gas Turbines Power, **134**(12), p. 122503.

[25] Childs, D. W., and Wade, J., 2004, "Rotordynamic-Coefficient and Leakage Characteristics for Hole-Pattern-Stator Annular Gas Seals - Measurements Versus Predictions," ASME J Tribol., **126**(2), pp. 326-333.

[26] Li, J., Li, Z., and Feng, Z., 2012, "Investigations on the Rotordynamic Coefficients of Pocket Damper Seals Using the Multifrequency, One-Dimensional, Whirling Orbit Model and RANS Solutions," ASME J Eng. Gas Turbines Power, **134**(10), pp. 102510.

[27] Vannini, G., Cioncolini, S., Del Vescovo, G., and Rovini, M., 2014, "Labyrinth Seal and Pocket Damper Seal High Pressure Rotordynamic Test Data," ASME J. Eng. Gas Turbines Power, **136**(2), pp. 022501.

[28] Li, Z., Li, J., and Feng, Z., 2015, "Numerical Investigations on the Leakage and Rotordynamic Characteristics of Pocket Damper Seals—Part I: Effects of Pressure Ratio, Rotational Speed, and Inlet Pre-swirl," ASME J. Eng. Gas Turbines Power, **137**(3), pp. 032503.

[29] Vannini, G., Bertoneri, M., Nielsen, K. K., Iudiciani, P., and Stronach, R., 2015, "Experimental Results and Computational Fluid Dynamics Simulations of Labyrinth and Pocket Damper Seals for Wet Gas Compression," ASME J. Eng. Gas Turbines Power, **138**(5), pp. 052501.

[30] Cangioli, F., Vannini, G., and Chirathadam, T., 2020, "A Novel Bulk-Flow Model for Pocket Damper Seals," ASME J. Eng. Gas Turbines Power, **142**(1), pp. 011012.

[31] Rouvas, C., and Childs, D. W., 1993, "A Parameter Identification Method for the Rotordynamic Coefficients of a High Reynolds Number Hydrostatic Bearing," ASME J Vib Acoust, **115**(3), pp. 264-270.

[32] ANSYS, 2016, "ANSYS Fluent User's Guide 17.2," ANSYS Inc., Canonsburg, PA.

[33] Yang, J., San Andrés, L., and Lu, X., 2019, "Leakage and Dynamic Force Coefficients of a Pocket Damper Seal Operating Under a Wet Gas Condition: Tests Versus Predictions," ASME J. Eng. Gas Turbines Power, **141**(11), pp. 111001.

[34] Picardo, A. M., 2003, "High Pressure Testing of See Through Labyrinth Seals," Master thesis, Texas A&M University, College Station, TX.

[35] Childs, D. W., 2020, Personal communication, April.

ACKNOWLEDGEMENTS

The support of the Turbomachinery Research Consortium is gratefully acknowledged. The authors thank the continued interest and encouragement of Dr. Dara Childs, Emeritus Professor of Mechanical Engineering and past Director of the Turbomachinery Laboratory at Texas A&M University.